Lab on a Chip

CRITICAL REVIEW

View Article Online
View Journal | View Issue

Cite this: *Lab Chip*, 2026, **26**, 1219

3D printing of droplet microfluidic devices: principles, wetting control, scale-up, and beyond

Je Hyun Lee,†[a] Taesoo Jang,†[a] Soeun Park,[b] Su-Bin Shin,[b] Jaemoon Lee,[b] Yoon-Ho Hwang*[b] and Hyomin Lee*[a]

Received 30th October 2025,
Accepted 12th January 2026

DOI: 10.1039/d5lc01011j

rsc.li/loc

3D printing is reshaping droplet microfluidics by converting digital designs into sealed, volumetric devices that integrate non-planar droplet generators and junctions, as well as embedded distributors. This Critical Review distills design rules that link geometry, key dimensionless groups (Ca, φ, λ), and wetting control to the robust production of single and multiple emulsions. We compare 3D printing modalities using criteria specific to droplet microfluidics, attainable feature size, optical clarity, chemical resistance, surface roughness, native wettability, and cleanability, and provide practical guidance on material–fluid compatibility, extractables, and long-run stability. We formalize scale-up *via* hydraulic balancing and unit-resistor strategies that preserve monodispersity across arrays, and outline selective surface treatments and multi-material printing approaches for achieving durable wettability patterns. Finally, we highlight AI/digital-twin workflows for predictive design and adaptive control, and map pathways toward standardized, manufacturable devices. These principles offer a conservative, application-oriented blueprint for 3D-printed droplet microfluidic devices.

1. Introduction

Emulsions, a colloidal system in which one fluid is dispersed as droplets within another immiscible fluid, are fundamental to a broad range of applications, including drug delivery, diagnostics, food, cosmetics, and advanced materials synthesis.[1–6] Despite their broad applicability and functional versatility, the lack of scalable production technologies with precise size control continues to hinder their industrial translation. Conventional bulk emulsification methods, such as mechanical stirring or homogenization, typically yield highly polydisperse droplets due to the limited control over the spatial and temporal distribution of shear forces during the emulsification process.[7]

In contrast, droplet microfluidic systems offer a powerful alternative, enabling precise manipulation of multiphase flows at the micro- to nanoliter scale to generate monodisperse emulsion droplets with well-defined sizes.[8,9] More importantly, such systems facilitate the generation of structured multiple emulsions including double- and even higher ordered emulsion droplets with high uniformity and architectural precision, broadening their utility in advanced encapsulation and templating applications.[10,11] In particular, single- or multi-layered microfluidic devices based on flow-focusing, T-junction, co-flow, and step geometries have been employed to produce such complex emulsions.[12] However, despite these numerous advantages, the broader implementation of microfluidic droplet generators has been hindered by limitations in material compatibility, fabrication complexity, and scalability.[13]

In response to these challenges, 3D printing, or additive manufacturing, offers cost-effectiveness, user-friendly operation, rapid one-step prototyping, and defect-free complex 3D geometry.[14,15] Recently, advances in techniques such as stereolithography (SLA), digital light processing (DLP), and two-photon polymerization (TPP) have enabled the fabrication of enclosed microchannels with sub-100 μm resolution, thereby expanding the design freedom and accuracy for the facile generation of emulsion droplets with a broad range of sizes.[16–18] Within the field of droplet microfluidics, 3D-printed devices have successfully replicated conventional geometries such as T-junctions and flow-focusing structures, while also facilitating advanced configurations including coaxial and multilayer emulsifiers.[19]

Indeed, most existing reviews in this field have primarily focused on fabrication technologies, with specific emphasis on printing resolution, hardware platforms, and device prototyping.[20,21] While these aspects are critical, practical considerations such as the compatibility of 3D printing

[a] *Department of Chemical Engineering, Pohang University of Science and Technology (POSTECH), Pohang 37673, Republic of Korea. E-mail: hyomin@postech.ac.kr*
[b] *Department of Polymer Engineering, Pukyong National University (PKNU), Nam-Gu, Busan 48513, Republic of Korea. E-mail: yoonho0806@pknu.ac.kr*
† These authors equally contributed to this work.

resins with the working fluids and the modulation of channel surface wettability through surface treatments to ensure stable flow dynamics and reliable droplet formation have received relatively limited attention.[22,23] Moreover, prior reviews have provided limited integration across flow physics, wetting/surface treatments, and materials compatibility in the context of 3D-printed droplet microfluidics. Furthermore, the potential of 3D printing to enable device modularity, parallelization, and scalable translation has not been comprehensively explored in the context of functional and application-driven microfluidic design.

This review aims to bridge these gaps by offering a comprehensive perspective on 3D-printed microfluidic platforms for emulsion generation (Scheme 1). We examine how key factors including resin material selection, wettability control, multichannel and parallelized device architecture, and throughput scaling, affect device performance and application potential. We further highlight emerging use cases, such as compartmentalized biological assays, organoid encapsulation, and soft material templating, which require customizable and dynamically tunable droplet production capabilities.

Lastly, we consider the prospective role of artificial intelligence (AI) in the device design optimization and digital workflow automation, pointing toward a future where droplet microfluidics evolve from static structures to adaptive, function-oriented systems. By integrating perspectives from materials science, fluid dynamics, and advanced manufacturing, this review aims to offer a comprehensive roadmap for researchers seeking not only to fabricate microfluidic droplet generators, but also to advance them toward scalable, robust, and application-oriented technologies.

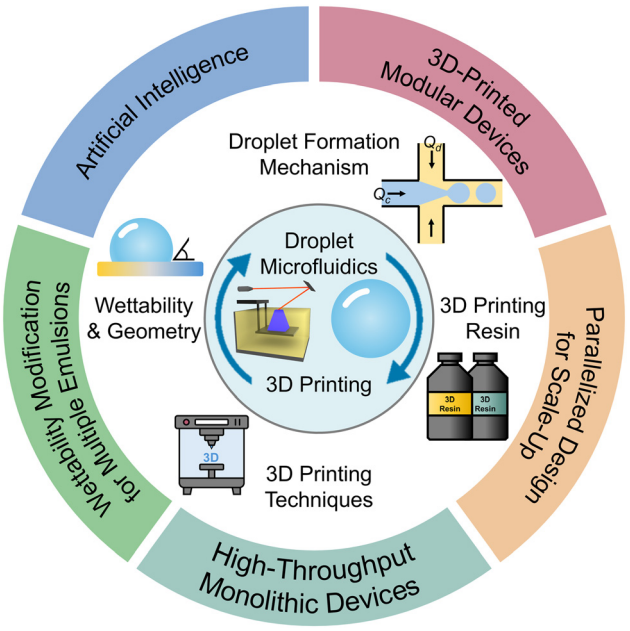

Scheme 1 Overview of the 3D-printed droplet microfluidic devices.

2. Fundamentals of emulsion generation in microfluidic devices

As outlined in the Introduction section, translating 3D-printed devices into reliable and scalable emulsion generating platforms benefits from a clear understanding of the underlying microfluidic physics. Microscale channels within such devices commonly operate in the low-Reynolds-number regime ($Re = \rho UD/\mu \ll 1$) where inertial force is negligible compared to viscous forces and thus the fluid flow is laminar.[24,25] In this regime, viscous stress and interfacial tension govern transport and breakup of dispersed phase. The capillary number ($Ca = \mu U/\gamma$), viscous stress scaled by surface-tension stress, together with the viscosity ratio ($\lambda = \mu_d/\mu_c$), the volumetric flow-rate ratio ($\phi = Q_d/Q_c$) between the dispersed (d) and continuous phases (c), and channel geometry, all provide a compact parameter set for regime and droplet size selection. As interfacial stresses and pressure gradients are well-controlled in confined flows, droplet pinch-off is effectively deterministic and resulting emulsions typically exhibit low coefficients of variation (CV).

By contrast, bulk mixing imposes nonuniform, transient shear and therefore produces broad size distributions. Droplet microfluidics overcomes this limitation by co-flowing two immiscible phases (*e.g.*, water/oil) in geometries that focus and neck the dispersed phase until capillary instabilities trigger breakup. The resulting droplets form continuously and behave as isolated microreactors with minimal cross-talk. Stable operation rests on three ingredients: (i) a workable interfacial tension (γ) set by the use of appropriate surfactants, fluid composition, and temperature, (ii) hydrodynamic forcing that places the device in the intended regime through absolute flow rates and their ratio (ϕ), and (iii) sufficient wall–phase selectivity to keep the breakup location and mode consistent over time. Indeed, recent work couples these rules with three-dimensional architectures to broaden operating windows and throughput. In particular, 3D-printed droplet microfluidics provides rapid, mask-free access to complex channel layouts, out-of-plane elements, and parallelized networks that preserve the deterministic breakup essential for achieving monodispersity while enabling robust and scalable droplet production across broader flow and material spaces. In the following subsections, we formalize passive breakup mechanisms and the governing non-dimensional controls, establishing design rules that later sections translate into 3D-printed architectures for generating single and multiple emulsions.

2.1. Droplet formation mechanisms

Droplet formation arises from an interfacial instability between two immiscible fluids that can break up in a controlled manner by the operating conditions as well as channel geometry.[26,27] Breakup is governed by the balance among viscous shear, interfacial tension, and capillary pressure. Interfacial tension resists deformation of the

dispersed phase, viscous stresses promote necking and pinch-off, and capillary pressure, which scales with surface tension over the local radius of curvature, sets the pressure drop that drives neck thinning and ultimately fixes droplet size. The resulting size, uniformity, and monodispersity are determined by the coupled effects of these stresses together with confinement, fluid properties, and flow-rate ratios. Above-mentioned dimensionless groups such as Ca, λ, and, when inertia becomes relevant at high throughputs or larger features, Weber number (We = $\rho U^2 D/\gamma$) provide compact descriptors of the governing regimes.[28,29]

Approaches to induce breakup can be either active or passive. Active devices apply external fields such as electric, magnetic, acoustic, optical, or centrifugal to modulate interfacial stresses in real time. Several dedicated reviews cover active control in depth,[12,30–33] and we therefore focus here on passive architectures to derive generalizable design rules for 3D-printed systems. Four canonical geometries dominate practice (Fig. 1A and B): T-junctions transition from confinement-driven squeezing at low Ca to shear-controlled dripping as Ca increases. Flow-focusing constrictions impose strong extensional and shear fields that stabilize periodic pinch-off across wide operating windows. Co-flow arrangements rely on axial shear and pressure gradients along a coaxial interface, with a well-defined shift from dripping to jetting as the continuous-phase velocity rises. Step emulsification is triggered primarily by a confinement transition at a sudden depth increase, where a Laplace-pressure jump sets breakup with a droplet size largely determined by inlet height and only weakly dependent on flow within its stable window, making it well-suited for robust parallelization.

2.1.1. Flow regimes according to operating conditions. Before detailing specific generation mechanisms governed by the channel geometry, it is useful to define the flow regimes that emerge from the interaction of the dispersed and continuous phases in confined microchannels. In the Stokes-flow limit, flow regime is dictated by viscous–capillary competition rather than inertia and is governed primarily by Ca, ϕ, λ, and geometric confinement.[29,34] At very low Ca and sufficiently large ϕ, squeezing occurs (Fig. 1A(i)). The dispersed plug periodically occludes the junction, upstream pressure rises, and a confinement-induced Laplace pressure difference expels a droplet. As Ca increases, the system enters dripping regime, where the local shear and extensional stresses overcome interfacial tension at the orifice and size decreases monotonically with increasing Ca or stronger focusing (Fig. 1A(ii)).[28,35] At higher Ca, a continuous filament forms and breaks downstream by Plateau–Rayleigh instability, producing jetting with sizes set by the jet diameter and the most unstable wavelength (Fig. 1A(iii)).[36,37] In the limit of very low γ or strong convective stabilization, two streams can persist in laminar co-flow without droplet formation (Fig. 1A(iv)). For a fixed fluid pair and geometry, the flow-rate ratio ϕ is the most direct dial for size. Increasing the continuous-phase flow at fixed dispersed-phase flow reduces diameter and increases frequency, whereas increasing the dispersed-phase flow at fixed continuous-phase flow enlarges droplets and can push operation toward squeezing or jetting. Meanwhile, the channel geometry repositions regime boundaries. Narrow throats and abrupt expansions favor squeezing or step-emulsification, while well-designed contractions favor wide, stable dripping windows. In practice, mapping (Ca, ϕ) for a given geometry provides a concise operating chart that targets droplet size and CV while avoiding undesirable transitions.[35,38,39]

2.1.2. Comparison of passive droplet generators. Each passive architecture shapes the same viscous–capillary

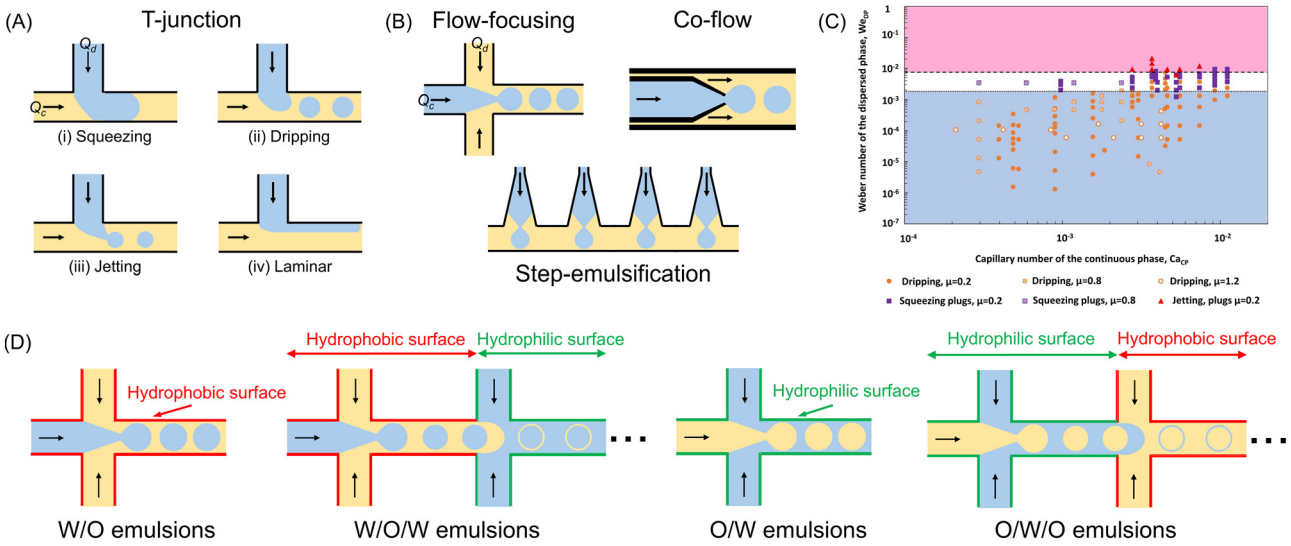

Fig. 1 (A) Fluid breakup dynamics and flow regimes in T-junction microfluidic devices. (B) Schematic illustration of other passive droplet generation methods in microfluidics. (C) Plot showing the effect of Capillary number of the continuous phase (Ca_c) and Weber number of the dispersed phase (We_d) on the flow regime. This figure has been reproduced from ref. 45 with permission from Elsevier, Copyright 2022. (D) Schematic illustrations of the channel wettability patterning process for generating single and double emulsions.

balance with a distinct stress field and thus exhibits characteristic performance envelopes (Fig. 1A and B). In T-junctions, confinement dominates at low Ca and larger ϕ, yielding squeezing. As Ca rises, shear-driven dripping takes over, typically with sizes limited by channel width and CVs of a few percent. Flow-focusing constricts a central dispersed stream with two sheath flows through a narrow orifice (Fig. 1B). Orifice width, aspect ratio, and contraction shape are first-order design parameters, and sizes from a few to about 200 micrometers are routine.[40,41] Under high ϕ and low γ with suitable surfactants, tip-streaming can access micrometer droplets at high frequency within a narrow stability window. Co-flow devices produce droplets near the orifice at moderate Ca and transition to jetting further downstream as the continuous-phase velocity increases.[37,42] Higher continuous-phase viscosity stabilizes dripping, whereas higher dispersed-phase viscosity promotes jetting, with practical size ranges of roughly 20 to 200 micrometers.[37,43] Step emulsifiers set size largely by inlet height and are comparatively flow-insensitive within their stable regime until a critical Ca is exceeded, making them ideal for parallelization by maintaining excellent size monodispersity across broad ranges.

2.2. Governing physicochemical factors

Emulsion generation reflects the interplay of interfacial tension, viscous stress, and, in limited cases, inertia, under geometric confinement and a specified wetting state. Interfacial tension γ sets the Laplace pressure ($\Delta p = \gamma(1/R_1 + 1/R_2)$) and dominates at small scales, controlling pinch-off, satellite formation, and stability.[39,44] Practical levers for γ include surfactant type, concentration, temperature, and solvent composition. As adsorption kinetics render γ dynamically during necking, transient Marangoni stresses can also delay breakup or shift regime boundaries when adsorption is slow relative to hydrodynamic thinning. The dimensionless controls, Ca, λ, and ϕ set the regime and the resulting droplet size by governing neck-thinning rates and pressure build-up. Inertia, usually negligible, can matter at higher throughputs or larger features, where We destabilizes dripping (Fig. 1C).[45]

On the other hand, wettability and confinement together determine which phase resides at the wall and set the local curvature field. Advancing and receding contact angles are more predictive than static angles because hysteresis captures pinning and history effects. Practically, a minimal specification that includes target Ca, λ, ϕ, the intended wetting state, and a geometry that fixes curvature and residence time is usually sufficient to predict regime and size, provided validation accounts for surfactant partitioning and aging as well as measurements on dynamic contact angles where possible.

2.3. Importance of wettability and channel geometry

Building on the physicochemical balances outlined above, reliable droplet generation requires a surface wettability that selects the intended continuous phase and a geometry that fixes local curvature and pressure jumps. Wettability is quantified by the liquid–solid contact angle and, more usefully for operation, by contact-angle hysteresis.[46] The continuous phase must preferentially wet the channel walls; otherwise, films of the dispersed phase form, the interface pins, and the device drifts toward coalescence or phase inversion. For instance, the oil should wet the walls while water remains nonwetting for water-in-oil (W/O) emulsion, whereas the opposite is required for an oil-in-water (O/W) emulsion. In flow-focusing devices, a critical contact angle near 92° is often cited for the transition between O/W and W/O operation, thus tuning the wall energy relative to the fluid pair is essential not only to establish the desired mode but also to broaden the stable dripping window and to suppress size drift.[47,48]

Multiple emulsions impose stricter spatial control because wetting preference must invert between stages and the boundaries must remain stable in the presence of surfactants (Fig. 1D).[48,49] A wide toolkit exists for setting hydrophilic or hydrophobic states, chosen to match the substrate and fabrication route. In polydimethylsiloxane (PDMS) soft lithography, oxygen plasma, poly(vinyl alcohol) (PVA) coatings, surfactant conditioning, and UV activation are common for hydrophilization, while silanization and fluoropolymer coatings provide durable hydrophobicity.[50–56] In silicon or glass MEMS (micro-electro-mechanical systems), photolithography with hydrophilic or hydrophobic silanes,[57–59] UV or electron-beam induced grafting,[60–62] and self-assembly of silica or fluorinated silica nanoparticles are typical.[63] In milled or laser-ablated plastics, oxygen plasma,[64] hydrophilic silanes,[65] and photografted polymers[66] are used for hydrophilic states, and hydrophobic silanes or fluorinated nanoparticle layers for water-repellent finishes. Glass capillaries are intrinsically hydrophilic and are usually rendered hydrophobic by silanization or by attaching hydrophobic molecules.[55,67] In 3D printing, post-print methods such as UV post-treatment,[23,68] silanization,[69] plasma activation,[70,71] thin-film coatings,[72] masking,[69] and flow patterning[68] are effective. Regardless of method, durability under flow and surfactant exposure should also be verified.

Geometry couples directly to hydrodynamics and therefore to size control and regime selection. Width and height set hydraulic resistance and confinement. Orifice width, contraction profile, and step height determine the stress distribution at breakup. Cross-sectional shape and surface roughness affect contact-line mobility and, therefore, the reproducibility of pinch-off. Effective designs should co-optimize these elements, selecting the simplest durable surface state that broadens the usable (Ca, ϕ) window while shaping the junction to localize the stress balance where deterministic breakup is desired.

2.4. Implication for device design

The required combination of channel geometry and surface wettability depends directly on the target emulsion. For single emulsions (O/W or W/O), constraints are modest: once

a breakup geometry is selected and throats or contractions are sized to meet diameter and throughput targets, a uniform surface state that favors the continuous phase typically suffices. Double (water-in-oil-in-water (W/O/W), oil-in-water-in-oil (O/W/O)) and higher-order emulsions demand stricter geometric staging and spatially resolved wetting. Junction spacing, cross-sectional transitions, and local height differences must be coordinated with a durable wetting sequence so that the continuous phase contacts the wall first at each stage; spacing should allow shell relaxation without promoting misalignment or coalescence.[73,74]

Translating complex emulsions from the laboratory to production requires uniform flow delivery and consistent surface treatment across many channels. These scale-out constraints expose limitations of several conventional methods. In PDMS soft lithography, oxygen plasma temporarily renders surfaces hydrophilic, but low-molar-mass oligomers migrate and restore hydrophobicity within hours; PDMS also swells in many organic solvents and exhibits thermal expansion during molding, which compromises dimensional stability.[75–77] In silicon or glass MEMS, repeated photolithography, silane deposition, and etching steps are needed for wettability patterning, which increases alignment burden and cycle time and can reduce yield.[78] In milled or laser-ablated plastics, manual mask realignment for multi-step patterning broadens boundary regions and introduces positional error.[79] Glass capillaries remain attractive for axisymmetric flows but cannot readily realize complex internal manifolds and can be vulnerable to solvents at adhesive joints.[80]

3D printing alleviates many of these issues by enabling volumetric routing, stacked junctions, and embedded distributors without layer registration, while introducing its own requirements including resolution anisotropy, resin swelling or extractables, and pressure-cycle durability that must be validated with the actual fluid and surfactant set, so that the deterministic breakup demonstrated in a single channel is preserved across arrays.

3. 3D printing for droplet microfluidics

While soft lithography remains efficient for rapid, inexpensive prototypes, its planar nature and PDMS material limits complicate out-of-plane features, long solvent duty, and uniform performance in large arrays. 3D printing offers true volumetric design freedom aligned with the operating logic in section 2. By shaping curvature and shear in three dimensions and embedding distributors and manifolds within the device body, 3D printing preserves deterministic pinch-off in well-designed junctions while enabling practical parallelization and high throughput.

The practical use of 3D printing in droplet microfluidics is set by more than nominal resolution. Optical clarity at imaging wavelengths, internal surface roughness and stair-stepping, dimensional fidelity under pressure and solvent exposure, and the feasibility of clearing supports from enclosed conduits, all feed directly into whether the resulting droplet size and its distribution are held consistent over time and across different channels. Another important aspect is the material interactions with the 3D printed matrices. Printed matrices can swell or leach low-molar-mass species in contact with oils, co-solvents, or surfactant-laden phases, which shift wetting and narrow the stable window of Ca and ϕ. However, employing appropriate post-cures, barrier coatings, and surface wettability modification methods can potentially resolve these issues by stabilizing the interfacial physics highlighted in the previous section. Moreover, orientation, layer thickness, and exposure strategy influence overcure through the depth and voxel anisotropy, which in turn set edge sharpness at orifices and steps where curvature jumps are prescribed. These fabrication choices may translate directly into working rules for robust production of single and multiple emulsions.

Another key advantage of 3D printing lies in the fact that it also enables system-level integration. Stacked drop makers fed by embedded resistive networks, out-of-plane crossovers that avoid footprint penalties, and modular couplings to sensors, heaters, or electrodes can be produced from a Computer-Aided Design (CAD) model. Iteration cycles can be potentially compressed down from several weeks to hours, which allows parameter sweeps in which Ca, ϕ, and λ are tuned alongside orifice width, step height, and manifold resistance. In this sense, 3D printing is not only an alternative to soft lithography but a complementary platform for translating droplet generators from concept to manufacturable hardware.

3.1. Overview of 3D printing techniques

American Society for Testing and Materials (ASTM) classifies additive manufacturing into seven categories (Fig. 2).[81] For enclosed microchannels and droplet generators, the most relevant are vat photopolymerization and material extrusion with material jetting and powder-based processes used for specialized parts or hybrid builds.

Vat photopolymerization includes stereolithography (SLA), digital light processing (DLP), and two-photon polymerization (TPP). These methods cure liquid resins with patterned light and are well suited to clear, enclosed channels at small feature sizes (Table 1).[82–88] SLA scans a laser to draw each layer and offers fine vertical control with smooth internal walls. DLP cures an entire layer in one exposure and usually prints faster while retaining similar in-plane resolution. TPP writes within the resin volume by nonlinear absorption and reaches down to submicrometer resolution, which is useful for specialty nozzles or master templates, although slow in printing speed for use in large devices.

Material extrusion is represented by fused deposition modeling (FDM). A thermoplastic filament is melted and deposited along toolpaths that define shells and infill. Resolution is set by nozzle diameter and bead geometry, yet

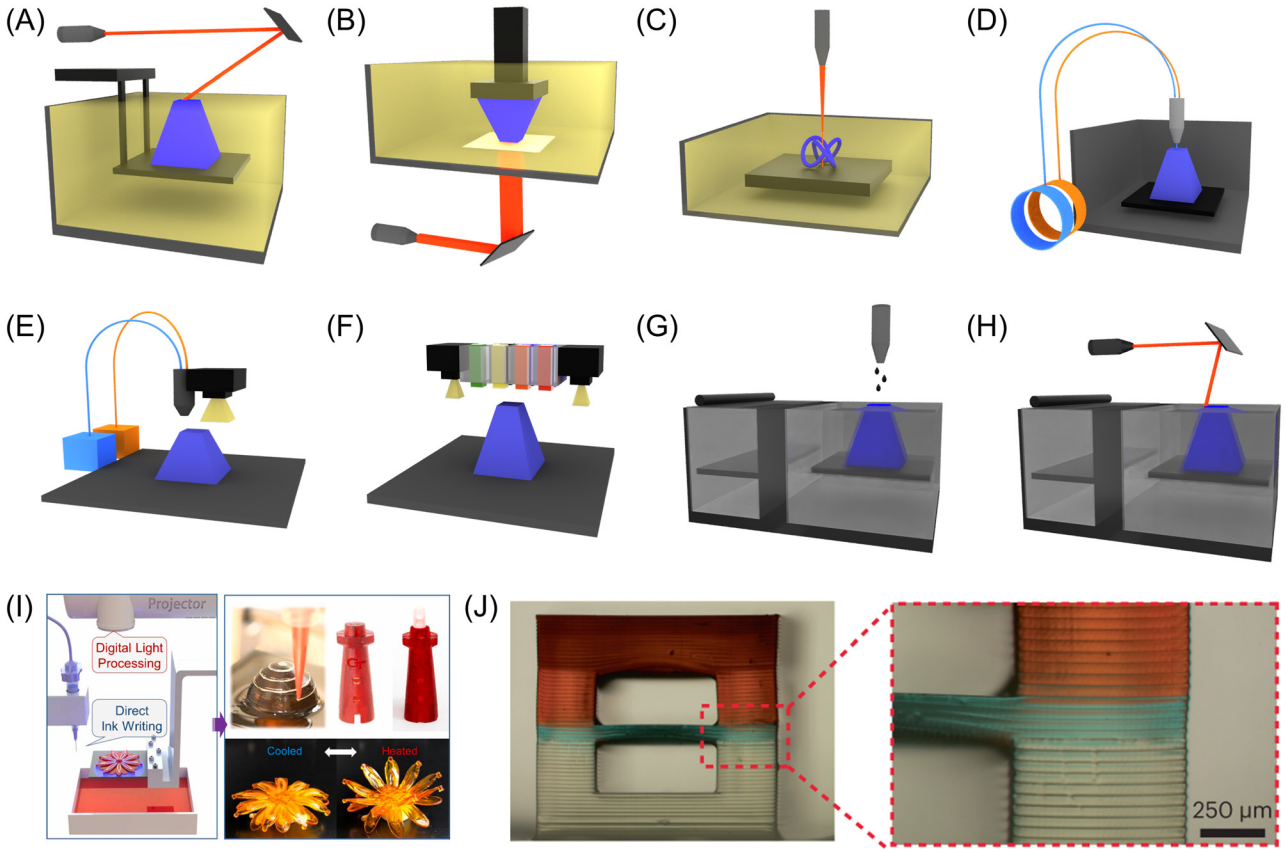

Fig. 2 Schematic illustrations of various 3D printing techniques. A) Stereolithography (SLA). B) Digital light processing (DLP). C) Two-photon polymerization (TPP). D) Fused deposition modeling (FDM). E) Material jetting. F) PolyJet. G) Binder jetting. H) Selective laser sintering (SLS). I) Hybrid process. This figure has been reproduced from ref. 141 with permission from Elsevier, Copyright 2021. J) Print–pause–print (PPP) method. This figure has been reproduced from ref. 142 with permission from Springer Nature, Copyright 2023.

Table 1 Commercially available DLP/SLA 3D printing resins that have been used for droplet microfluidic applications. The table summarizes reported achievable feature sizes, optical transparency, and compatible oil–surfactant systems. The references next to each resin name indicate the corresponding suppliers

Resin name	Feature size	Optical transparency	Compatible oil & surfactants	Used in
Accura 60 (ref. 82)	1.58 mm × 8 mm pyramidal void	Transparent	Hexadecane (span 80, 2 wt%)	177
RLV-1 (ref. 83)	74 μm × 75 μm channels	Transparent	Mineral oil (span 80, 2 wt%)	104
HTL (ref. 84)	80 μm channels	Transparent	Mineral oil (span 80, 4.5 wt%)	105
	70 μm × 70 μm channels	Transparent	Mineral oil (span 80, 2 wt%)	176
R11 (ref. 85)	60 μm × 60 μm channels	Transparent	Paraffin oil/heptane (span 80, 2 wt%)	169
	150 μm channels	Opaque	Hexadecane (span 80, 1.5 wt%)	190
PIC100 (ref. 85)	50 μm channels	Translucent	Hexadecane (span 80)	174
eShell600 (ref. 85)	200 μm channels	Translucent	Mineral oil/heptane (span 80)	194
Clear (ref. 86)	600 μm axisymmetric co-flow	Opaque	Mineral oil (span 80, 4 wt%)	179
	150 μm channels	Translucent	Silicone oil (Dow corning 749)	191
BV-003 (ref. 87)	1.58 mm channels	Transparent	Hexadecane/dodecane (span 80 + span 20)	186
WaterShed XC 11122 (ref. 88)	500 μm channels	Transparent	Halocarbon oil 4.2	188

extrusion remains inexpensive and robust, so it is practical for manifolds, housings, fixtures, and simple millimeter-scale channels. It also integrates well with solvent bonding or lamination in hybrid assemblies that include transparent channel layers. Material jetting ejects droplets of photocurable resin from nozzle arrays and cures them immediately. It supports multi-material blends and yields smooth surfaces and clear windows, but enclosed-channel design requires attention to support strategies. Powder bed fusion forms strong parts from polymer powders with the surrounding bed providing self-support. It excels at complex mesoscale structures and rugged housings but has higher porosity and roughness than photopolymer methods, which complicates sub-millimeter enclosed channels unless walls

are sealed or infiltrated. Binder jetting patterns a liquid binder onto powder layers at room temperature and then relies on post-processing for densification. It is fast and economical for large components but faces similar limits for fine enclosed features and solvent-tight channels.

In practice, selection turns on a few recurring needs. The modality must form sharp throats, steps, and orifices at the target scale. Internal walls should be smooth and optically clear at imaging wavelengths. Supports and uncured material must be cleared from enclosed voids, and the printed polymer or resin must remain compatible with the intended oils, aqueous phases, and surfactants after post-cure (Table 1). With these criteria in view, the following subsections outline each technique's operating principles, controllable variables, and post-processing steps, emphasizing how they preserve breakup-site geometry, wetting stability, and array-level uniformity.

3.1.1. Stereolithography (SLA). SLA, first introduced by Chuck Hull in 1986, employs a UV laser to selectively cure photo-reactive liquid resins in a layer-by-layer fashion, producing solid structures with high resolution and smooth surface finish (Fig. 2A).[17,89] Following layer curing, the build platform is incrementally displaced, followed by replenishment with fresh resin, and this cycle is repeated until the final structure is completed. Post-processing typically involves rinsing with isopropyl alcohol (IPA) and UV post-curing to enhance the mechanical strength and dimensional stability.

Resins for SLA consist of photo-reactive monomers, photoinitiators, and additives. The curing depth is governed by optical properties such as absorption and scattering, following the Beer–Lambert law.[90,91] Rheological behavior, particularly viscosity, also influences printability. Acrylate- and epoxy-based systems are widely used, with hydrogel-based formulations (*e.g.*, poly(ethylene glycol) diacrylate (PEGDA), gelatin methacrylate (GelMA)) offering biocompatibility for bioprinting applications.[92–94] Common photoinitiators include bis(2,4,6-trimethylbenzoyl)phenylphosphine oxide (BAPO), Irgacure derivatives, and trimethylbenzoyl diphenylphosphine oxide (TPO), which are responsive to either UV or visible light.[95]

In terms of achievable spatial resolution, SLA allows resolutions down to ~27 μm in the *XY* plane and 0.25 μm along the *Z*-axis, sufficient for fabricating microchannels with dimensions <20 μm.[95–98] For instance, Gong *et al.* achieved channels of 18 × 20 μm by employing light-absorbing additives and edge exposure strategies.[99] SLA-printed templates have also been applied in hot embossing for capillaric circuits (CCs), demonstrating low-cost and rapid prototyping (<$15 within 48 h). Similarly, Au *et al.* fabricated fully integrated plastic valves and pumps using SLA, achieving pressures of 1–6 psi and flow rates up to 0.68 mL min^{-1}, thereby overcoming the limitations of PDMS-based systems.[100] However, despite its popularity, SLA is often limited by relatively slow throughput due to its layer-by-layer curing process, as well as by constraints in resin diversity and long-term biochemical compatibility. Ongoing research into expanding the library of applicable resin materials and scalable strategies is expected to broaden its applicability in droplet microfluidic device manufacturing.

3.1.2. Digital light processing (DLP). DLP employs a digital micromirror device (DMD) chip to project patterned light onto photo-reactive resins, curing an entire layer in a single exposure (Fig. 2B). As in SLA, the process is repeated layer-by-layer, followed by post-processing steps such as washing, UV curing, and support removal. Compared to SLA, DLP offers two distinct advantages: (i) faster printing speed due to layer-wise curing, and (ii) reduced oxygen inhibition due to less exposure of the resin to air.

Epoxy- and acrylate-based polymers remain the most common resin systems, though hydrogels, ceramics, elastomers, and metallic suspensions have also been employed.[98,101,102] Performance can be tuned using photoinitiators, light-absorbing dyes, and additives for resolution enhancement. Resolutions of ~20 μm are typical, with feature sizes as small as 7 μm achieved using specialized photoinitiators such as diphenyl(2,4,6-trimethylbenzoyl)phosphine oxide.[103]

Several studies highlight the potential of utilizing DLP in microfluidics. Van der Linden and co-workers fabricated modular systems including filters, mixers, droplet generators, and traps by eliminating stray light above 400 nm and applying nanoscale filters to prevent clogging.[104] The entire device was produced within 15 min and was reusable after washing. Transparent enclosed chips have also been fabricated, enabling stable production of W/O emulsions at T-junctions and continuous analyte monitoring.[105,106] Importantly, surface wettability and roughness critically affect DLP-fabricated devices. Kang *et al.* demonstrated that increasing the stacking thickness (10, 50, 100 μm) increased surface roughness (0.38–7.03 μm) and altered wettability depending on the orientation.[107] Capillary-driven flow was most effective in vertically stacked channels at 10 μm, while excessive thickness degraded the device performance. These findings emphasize the importance of layer thickness and print orientation in governing flow characteristics. Overall, DLP provides faster throughput and finer resolution than extrusion-based methods, while also offering optical transparency suitable for on-chip observation. However, careful control of resin chemistry, stacking parameters, and surface characteristics are all required to ensure reproducible microfluidic performance.

3.1.3. Two-photon polymerization (TPP). TPP is a laser-based 3D printing technique that exploits nonlinear photon absorption (Fig. 2C). When a femtosecond near-infrared (NIR) laser is focused into a resin bath, simultaneous absorption of two low-energy photons excites the photoinitiator, generating reactive species that locally initiate polymerization.[16,108] As polymerization occurs only within the confined focal volume, features at the sub-micrometer scale can be achieved. Three-dimensional structures are fabricated by scanning and stacking voxels according to sliced CAD models, followed by post-processing such as solvent washing and UV curing.

TPP is compatible with a wide range of resins, provided they are transparent at NIR wavelengths and responsive to two-photon absorption. Acrylate-based systems are widely used owing to ease of processing and mechanical robustness, enabling applications in optics, scaffolds, and drug delivery.[16,109] In particular, hydrogel-based formulations, despite lower mechanical strength, are valuable for bioprinting and tissue engineering due to their biomimetic nature.[110] Organic–inorganic composites have been also applied to microneedles and scaffolds, offering biocompatibility and low shrinkage.[16,109,111,112] Epoxy-based systems, such as SU-8, remain less common due to complex post-processing, but have been demonstrated for their use in microfluidic devices.[113]

A key advantage of TPP is its ultrahigh resolution, reaching down to ~100 nm. Derived approaches such as direct laser writing (DLW) extend TPP's capabilities, enabling fabrication of complex 3D geometries not accessible by other methods and allowing integration with existing protocols. Despite these strengths, TPP suffers from slow printing speed and high system cost, which limit scalability and industrial adoption.[21,109,114–116] As a result, it remains primarily a research tool for applications requiring nanoscale precision rather than large-scale device manufacturing.

3.1.4. Fused deposition modeling (FDM). FDM, first introduced by Scott Crump in 1988, allows fabrication of 3D structures by heating and extruding thermoplastic filaments through a nozzle and depositing them layer-by-layer (Fig. 2D).[95] CAD models are converted into STL files, sliced into layers, and translated into G-code, which directs the nozzle to build the desired platform.[117,118] Each extruded filament solidifies upon cooling below its glass transition temperature (T_g), and the process is repeated until the final structure is formed. Post-processing, such as polishing or surface coating, can be also employed to improve surface finish.

Thermoplastic polymers including acrylonitrile butadiene styrene (ABS) and polylactic acid (PLA) are most commonly used owing to their favorable rheological properties. Amorphous polymers are generally preferred because of their lower warping and shrinkage during cooling, whereas semicrystalline polymers often introduce internal stress and dimensional instability. An additional advantage of FDM is its compatibility with recycled thermoplastic feedstocks, lowering both cost and environmental impact.

While FDM is among the most accessible and cost-effective 3D printing methods, offering low equipment cost and rapid prototyping capabilities, its resolution is fundamentally limited by nozzle diameter which is typically ~500 μm.[97,119,120] However, Romanov *et al.* recently demonstrated improved channel resolution (~300 μm) using a commercial FDM printer, fabricating enclosed channels (400 × 400 μm) with optical transparency sufficient for visualizing dye mixing and droplet generation.[121] PLA annealing further enabled applications in high-temperature analysis. Cost-effectiveness and modularity have also been leveraged to design droplet-on-demand systems. By integrating an FDM-printed nozzle module with a pipette tip, monodisperse droplets were generated with CV between 0.81–3.61% at flow rates of 50–150 μL min^{-1}.[122] The platform, costing ~$2500, enabled droplet storage through cartridge integration while avoiding the need for cleanroom fabrication or complex valve-based operation. Despite its low resolution and limitations in producing fine microstructures, FDM provides a useful trade-off between speed, simplicity, and cost, making it attractive for rapid prototyping, educational use, and low-cost modular microfluidic systems.

3.1.5. Material jetting. Material jetting is a 3D printing technique derived from inkjet printing principles (Fig. 2E). Specifically, photopolymers, waxes, or metal/ceramic suspensions are stored in reservoirs, heated, and dispensed through nozzles onto the build platform.[21,123] For instance, after deposition, each layer is cured by UV irradiation before the platform lowers for subsequent layers. Repetition of this cycle yields the final 3D structure. As liquid or molten resins are deposited, support structures are generally required and later removed through additional chemical treatment (*e.g.*, sodium hydroxide (NaOH) solution), thermal processing, or high-pressure water jetting.[123,124]

This method accommodates a wide range of materials, including thermosets, thermoplastics, elastomers, and composites. A distinguishing feature of material jetting is its broad-spectrum UV curing (190–400 nm), which allows use of various resin formulations. It also provides one of the finest resolutions among 3D printing methods, achieving layer thicknesses as low as 16 μm.[123,125]

Material jetting is therefore valued for its high precision, smooth surface finish, and compatibility with multi-material printing. However, reliance on support structures and relatively high material costs remain key challenges, particularly when scaling toward functional microfluidic device fabrication.

3.1.6. Photopolymerization jetting (PolyJet). PolyJet belongs to the material-jetting family based on the ASTM classification. During the PolyJet process, photocurable resin droplets are jetted through multi-nozzle arrays, deposited onto the build platform, and immediately UV-cured; the platform then steps down for the next layer (Fig. 2F). The technology supports simultaneous, voxel-level deposition of multiple formulations (*e.g.*, rigid–rubber blends, colored/transparent resins), enabling digital materials with tunable modulus and optical properties. Compared with SLA, PolyJet typically offers faster layer cycle times, high in-plane resolution (tens of micrometers) with excellent surface finish, and straightforward support generation for overhangs and enclosed cavities.[21,95,126,127]

In terms of its implication in microfluidic devices, the main advantage of PolyJet lies in optical clarity, multi-material integration (*e.g.*, rigid body with elastomeric valves), and rapid iteration of complex architectures. However, key limitations still remain: (i) support removal from narrow channels can be difficult and may leave residues; (ii) resin swelling or leaching can occur in contact with organic

solvents or surfactants; and (iii) thermal and chemical stability are lower than those of glass/ceramic systems, constraining long-term or harsh-chemistry operation. Strategies such as sacrificial ink filling, soluble support formulations, and post-print coatings (*e.g.*, parylene, silanization, or fluoropolymer layers) are often required to ensure clean, wettable channels suitable for robust droplet generation.[128–131]

3.1.7. Binder jetting. Binder jetting fabricates parts by selectively depositing a low-viscosity liquid binder onto sequential layers of powder, consolidating particles without in-process heat (Fig. 2G). After each 2D pattern is printed, the build platform lowers, a fresh powder layer is spread, and the cycle repeats until completion. As the surrounding loose powder acts as self-support, no additional support structures are required, enabling high build speeds and low cost for large or complex components. However, the binder must maintain stable jetting under shear and wet the powder uniformly to minimize defects.

While a broad range of feedstocks (polymers, ceramics, composites, and some metals with suitable post-processing) is compatible, the resolution and surface quality are often constrained by particle size, powder packing, and binder bleed, yielding higher porosity and roughness than photopolymerization methods.[21,132,133] For microfluidic applications, major challenges include powder removal from enclosed microchannels, dimensional fidelity of narrow features, and fluid leakage through the porous walls. Consequently, post-processing such as infiltration, curing, or sintering (which negates the initial no-heat advantage), is typically required to densify parts and improve chemical resistance. These factors currently limit binder jetting's use for fabrication of sub-millimeter microchannels and solvent-exposed droplet generators, though it remains attractive for rapid, low-cost meso-scale components and fixtures.

3.1.8. Selective laser sintering (SLS). SLS, pioneered by Deckard and Beaman (1986), is a powder bed fusion process in which a high-power laser selectively fuses powder particles within a preheated bed (Fig. 2H). Following 3D CAD preparation and slicing, the build chamber and powder are heated slightly below the polymer melting temperature (T_m) to narrow the required laser energy window and reduce thermal gradients. A scanning laser then locally sinters the patterned regions; after each layer, the platform lowers, a fresh powder layer is spread, and the cycle is repeated. Parts are subsequently cooled in-bed and subjected to post-processing including depowdering, thermal annealing, infiltration or sealing.

Typical feature resolution achievable using laser sintering is ~100 μm, governed by laser spot size, hatch spacing, and particle size distribution.[124] The unsintered powder acts as a self-supporting medium, enabling complex, overhanging geometries without dedicated supports and facilitating powder reuse for improved economics. Common feedstocks include nylon (PA12, PA11), thermoplastic polyurethane (TPU), and engineering thermoplastics; high-temperature polymers such as polyether ether ketone (PEEK) are also accessible with specialized hardware.[134,135]

Compared with photopolymerization methods, SLS parts exhibit higher porosity and surface roughness (tens of μm), which complicates the fabrication of sub-millimeter enclosed channels and can induce wetting heterogeneity, leakage, or fouling in droplet generators.[136–138] Dimensional fidelity is also sensitive to powder packing quality, particle size, and thermal behavior across the crystallization/melting window; even within a single polymer family, variations in molecular-weight distribution shift the sintering window and can lead to non-uniform neck growth, warpage, or incomplete fusion. Defects in powder spreading or bed uniformity therefore tend to print through as dimensional errors inside enclosed channels.

3.1.9. Hybrid process. As no single 3D printing modality can satisfy all the key specifications required for droplet microfluidic platforms, hybrid processes that combine multiple 3D printing methods and/or post-fabrication steps with conventional machining or bonding are often synergistically employed to offset modality-specific limitations while preserving their strengths.

A representative approach is the FDM–solvent-bonding route. Duong and Chen coupled FDM-printed ABS superstructures to polymethyl methacrylate (PMMA) substrates *via* solvent bonding, leveraging ABS for mechanical robustness, low-cost, and rapid prototyping while exploiting PMMA's optical transparency for on-chip imaging.[139] Solvent delivery by spray coating minimized solvent usage and cost, enabling structurally stable, optically accessible chips suitable for routine analysis. Another strategy integrates PolyJet printing with laser lamination/micromachining. Alapan and co-workers addressed support removal and surface finish challenges in PolyJet by (i) designing the manifold ends as open features to facilitate support extraction, followed by epoxy sealing, and (ii) stacking a three-layer assembly; a 3D-printed flow-distribution manifold (top), a micromachined channel layer (middle), and a glass substrate (bottom).[140] The resulting device exhibited high transparency, uniform channel geometry, and stable flow distribution, demonstrating its suitability for bioanalytical applications such as target cell isolation.

By integrating top-down DLP for high-speed, high-resolution polymer matrix fabrication with *in situ* DIW deposition of functional inks, a hybrid multi-material 3D printing method was shown to produce interfacially robust, tunable, and multifunctional devices such as soft robots, circuit-embedded structures, and strain sensors in a single build (Fig. 2I).[141] Also, the SLA-based print-pause-print (PPP) process was employed to print transparent PEGDA on a glass substrate to smooth the surface, after which the print is paused to swap resins, enabling alignment and stacking of dissimilar materials layers composed of PEGDA with different molecular weights (Fig. 2J).[142]

Together, these examples illustrate how hybridization can meet droplet-device requirements while revealing specific trade-offs. In practice, hybrid processes enable cost-effective

fabrication by reserving inexpensive 3D printing for bulk fixtures while assigning optical-grade microchannel layers to PMMA or glass; they improve cleanability and support removal by externalizing sacrificial materials before final sealing; and they permit tailored wettability or barrier properties through thin post-coatings or adhesive interlayers without sacrificing geometric fidelity. Remaining challenges include interfacial reliability (solvent or adhesive compatibility, creep resistance, and thermal-cycle robustness), tolerance stacking across disparate processes that can erode throat and step dimensions, and long-term chemical stability under surfactants or organic phases. Even so, when a single printing process falls short, well-designed hybrid schemes provide a pragmatic route to application-ready microfluidic hardware that maintains deterministic pinch-off and array-level uniformity.

3.2. Evolution of 3D printable resins for microfluidic systems

3D-printing resins for droplet microfluidic systems have evolved from general-purpose acrylates to formulations that are biocompatible, optically clear, and chemically resistant, yet still compatible with high-resolution photopolymerization. Early methacrylate systems prioritized cure speed and dimensional fidelity but often showed heterogeneous surface chemistry, autofluorescence, and extractables that interfered with interfacial control. Current resin families include low-autofluorescence acrylates,[124,143,144] epoxy,[124,144–146] and thiol–ene systems with reduced oxygen inhibition,[147,148] PEG- and GelMA-based hydrogels for biointegration,[144,148,149] as well as composite formulations that embed silica or ceramic nanoparticles to increase modulus and solvent resistance without sacrificing printability.[91,150,151]

Optical performance is a primary consideration when on-chip visualization is required. Resins with low scattering and refractive indices close to those of water or common oils improve image contrast and reduce lensing at channel walls. Low background fluorescence across the blue–green bands preserves assay sensitivity, and both photoinitiator choice and post-cure schedule strongly affect clarity and residual absorbance.

Chemical resistance has advanced through higher cross-link density, selection of less-swellable backbones, and partial monomer fluorination.[69,152–154] These strategies improve compatibility with hydrocarbon oils, silicone oils, and fluorinated oils, and they mitigate swelling that would otherwise alter channel dimensions and wetting properties. For biologically oriented workflows, medical- or research-grade resins emphasize low extractables and cytocompatibility after full post-cure and solvent rinse. As surfactants can partition into the matrix and alter interfacial tension and surface wettability over time, compatibility is increasingly addressed at the formulation stage and verified under representative flow conditions.

Overall, resin selection is guided by a balanced specification. Cytocompatibility after sterilization, high optical transmission with low autofluorescence, resistance to the intended continuous and dispersed phases and their surfactants, minimal swelling at operating temperature, and predictable cure kinetics that preserve small features and enclosed voids. Meeting these criteria stabilizes surface wetting and interfacial stresses, which in turn supports robust, low-drift droplet generation over an extended operation period.

3.3. Surface properties of 3D-printed microchannels

Improvements in bulk resin chemistry reduce swelling and extractables, but the as-printed interface still sets the initial wetting state and strongly influences long-term operation stability in droplet microfluidics. Most photopolymer prints present moderately hydrophobic walls with water contact angles that naturally favor W/O operation unless modified. At the microscale, layer lines and cure fronts produce chemical and topographic heterogeneity that manifests as contact-angle hysteresis (CAH), which can broaden droplet size distributions if not actively managed. Residual photoinitiator, unreacted monomer, and low-molar-mass oligomers may also leach into contacting fluids, depressing interfacial tension and driving gradual wetting drift during extended operation.

Surface roughness arises from voxelation, layer stepping, and overcure halos. Even when the arithmetic roughness is only a few hundred nanometers, sharp edges at junctions and steps can trap contact lines and promote pinning. This widens the gap between advancing and receding angles and ties local wetting to flow history, so interfacial energy is better characterized by hysteresis and dynamic angles than by static values alone. Low-energy, fluorinated surface skins stabilize W/O dripping with low hysteresis, whereas polar or silica-like barrier coatings favor O/W operation and reduce fouling; in both cases, fillets, gentle tapers, and controlled edge exposure help suppress pinning, and large arrays benefit from prior surface homogenization to limit outlet-to-outlet drift.

3.4. Robust operation of 3D-printed microfluidic systems

Building on the surface properties discussed above, long-run stability in droplet production is governed as much by chemistry at the solid–liquid boundary as by channel geometry. Three issues dominate extended operation: (i) interactions between the printed matrix and surfactants, (ii) solvent-induced swelling, and (iii) release of low-molar-mass species.

Nonionic surfactants used to stabilize W/O or O/W droplets can partition into the polymer network, lowering their effective bulk concentration and shifting equilibrium interfacial tension. In parallel, adsorption of surfactants or proteins alters wall energy and can nudge operation from dripping toward jetting or co-flow. In long manifolds and arrays, such local changes accumulate and may appear as outlet-to-outlet maldistribution.

Swelling depends on solubility-parameter proximity and crosslink density. A few percent volume change is enough to alter throat width or step height and to move regime boundaries and droplet size, especially in step emulsification devices. Epoxies and highly crosslinked acrylates generally resist swelling better than loosely crosslinked networks or hydrogels in hydrocarbon oils or fluorinated oils, whereas aqueous buffers can plasticize hydrophilic matrices. Early, accelerated screening with the intended oils and surfactants helps flag dimensional drift before full designs are committed.

Lastly, leachables including unreacted monomers, oligomers, photoinitiator fragments, and small additives can depress interfacial tension, interfere with assays, and reduce cell viability. Thorough wash and post-cure protocols, thin barrier layers such as parylene or silica, and cure schedules that drive high conversion mitigate these effects.

In practice, durable operation follows from pairing a resin that remains dimensionally stable in the target fluids with light-touch stabilization of the desired wetting state and verifying that the chosen build and post-cure preserve critical features at orifices and steps over the time scales relevant to deployment.

3.5. Opportunities and trade-offs of 3D-printed droplet microfluidics

Soft lithography and glass-capillary assemblies have driven much of the early progress in droplet microfluidics,[8,11,155–159] yet their planar or axisymmetric constraints limit uniform and scalable operation.[160,161] In PDMS, channels typically occupy a single plane, so distribution relies on two-dimensional manifolds where path-length disparities accumulate hydraulic resistance and desynchronize branch flows.[162] True out-of-plane control is difficult, which complicates precise pinch-off positioning, confinement transitions, and the placement of internal features such as undercuts, re-entrant cavities and vertical chimneys. On the other hand, glass capillaries provide tapered or coaxial alignment[158] but depend on manual assembly and operator skill, which reduces reproducibility and complicates integration.[163–165] These constraints inflate dead volume, increase hydrodynamic crosstalk and restrict practical parallelization.[17,166]

In this context, 3D printing opens intrinsically three-dimensional architectures that expand the functional design space rather than refining planar layouts.[97] Embedded manifolds can be routed above or below the active plane and reconnected by short vertical vias, which preserves in-plane real estate and enables compact stacked arrays.[99,167–169] Channel crossovers and overpasses eliminate same-plane intersections by briefly elevating one stream and returning it to height, removing long detours and junction dead volume.[170,171] Curved geometries such as spirals, arched junctions and gently tapered nozzles encode continuous curvature and axial taper in a monolith, which suppresses recirculation and stagnation that arise at sharp corners or abrupt area changes.[17,172–175] For instance, vertical step emulsifiers implement discrete height transitions within a single body, allowing immediate out-of-plane routing downstream of the step.[176,177] Nested coaxial nozzles fix concentricity by design and enable hierarchical droplets without manual capillary alignment.[131,178,179] Internal motifs such as caged junctions, meniscus anchors, satellite-capture pockets and bubble vents further stabilize long-run operation.[104,180] These capabilities translate into improved monodispersity, higher stability of multiple emulsions, scalable parallelization and robust continuous use.

To realize these advantages, geometry must be co-optimized with process physics at the design stage. Minimum feature size and anisotropy set limits on step height and edge acuity, so critical throats and steps should be oriented along the printer's highest-fidelity axis.[99] Enclosed voids require vent and drain pathways to avoid resin entrapment and incomplete cure, and small test coupons that replicate the tightest vias and deepest pockets help de-risk builds. Short vertical steps and vias benefit from gentle axial tapers that ease post-cure flushing and reduce print artifacts.[97] Layer texture can induce CAH and wetting defects, which are mitigated by local fillets, controlled overexposure, brief solvent reflow or conformal post-coatings at critical edges.[107] Optical performance depends on wall thickness and material transparency, so thin and uniformly cured windows placed around the imaging plane improve visualization.[181] Geometric choices should be coupled to resin chemistry and curing kinetics, including exposure dose, absorption and scatter, polymerization shrinkage and thermal history, since neglecting these interactions promotes warpage, microvoids, and unintended constrictions that compromise dimensional fidelity and flow stability.

A balanced comparison clarifies where each platform excels. For strictly planar designs replicated from a stable master, soft lithography offers superior in-plane edge acuity and low unit cost once tooling is in hand.[17,182] As a result, it still remains attractive for steady high-volume planar replication with stringent edge definition. For architectures that require out-of-plane manifolds, compact crossovers, vertical steps or coaxial nesting, and for systems that value rapid architectural iteration with array-level uniformity, 3D printing provides a more direct path from concept to manufacturable hardware. Photopolymer printers deliver features sufficient for typical nozzle throats and step heights while integrating three-dimensional distribution within a single build and reducing assembly variability.

Cost profiles also differ accordingly. PDMS becomes economical when many copies are cast from a mature master, whereas frequent redesign and progressive scale-out of complex layouts generally favor printed builds that avoid mask rework and multi-layer alignment.[183] Throughput also follows different levers. PDMS uses batch replication from one master, while 3D printing achieves build-level throughput by producing arrays and embedded manifolds in one job.[20]

Overall, platform choice follows from the geometry and lifecycle of the device rather than from a single headline metric. If the target is planar and stable in design, soft lithography remains a strong option. However, if the target relies on three-dimensional routing, stacked junctions and rapid iteration with uniform arrays, 3D printing would be the more natural route to reliable droplet generators.

4. Architectures and scale-up in 3D-printed devices

Conventional microfluidic droplet generators, including T-junctions, flow focusing, co-flow geometries, and step emulsifiers, provide a foundation for controlled droplet production for a wide range of applications including drug delivery, chemical synthesis, and materials engineering. With the advent of 3D printing, these canonical geometries can be realized reproducibly without cleanroom infrastructure or multi-step bonding, lowering the barrier to design iteration and comparative testing. In the sections to follow, we briefly review the recent advances made in 3D-printed droplet microfluidic devices with specific emphasis on design freedom beyond planar geometry, scale-up, as well as their applications.

4.1. Canonical droplet generators and 3D-printed advances

Recent studies have verified that 3D-printed versions of canonical geometries match the performance of soft-lithography or glass-capillary system counterparts when materials and wetting are properly controlled (Fig. 3). For instance, Morgan *et al.* improved accessibility by using low-cost fused filament fabrication to print T-junctions and flow-focusing devices, resolving typical limitations of this method such as leakage and limited optical transparency (Fig. 3A).[184] Using high-resolution stereolithography, Warr *et al.* showed that resin properties can be as critical as the channel geometry.[131] They demonstrated that stable production of W/O emulsions in cross-junctions required inherently hydrophobic resins and introduced a new hydrophobic formulation to achieve reliable performance.

Beyond replication of basic layouts, 3D printing uniquely enables complex monolithic structures that are difficult to realize with conventional assembly. Ghaznavi *et al.* reported an axisymmetric co-flow device that is traditionally built by manual alignment of fragile glass capillaries (Fig. 3B).[179] By printing the entire multi-nozzle co-flow structure as a single monolithic part, they eliminated the manual assembly procedure and achieved robust generation of both single and compound emulsions with precise concentric alignment. Step emulsifiers have also been realized using 3D printing. As detailed by Stolovicki *et al.*, step emulsification relies on a confinement transition and a Laplace-pressure jump at a sudden expansion rather than finely tuned shear, making the design tolerant to minor surface roughness and geometric variations that may occur in 3D-printed parts (Fig. 3C).[185]

Recent advances go further by leveraging true three-dimensional freedom to solve long-standing challenges

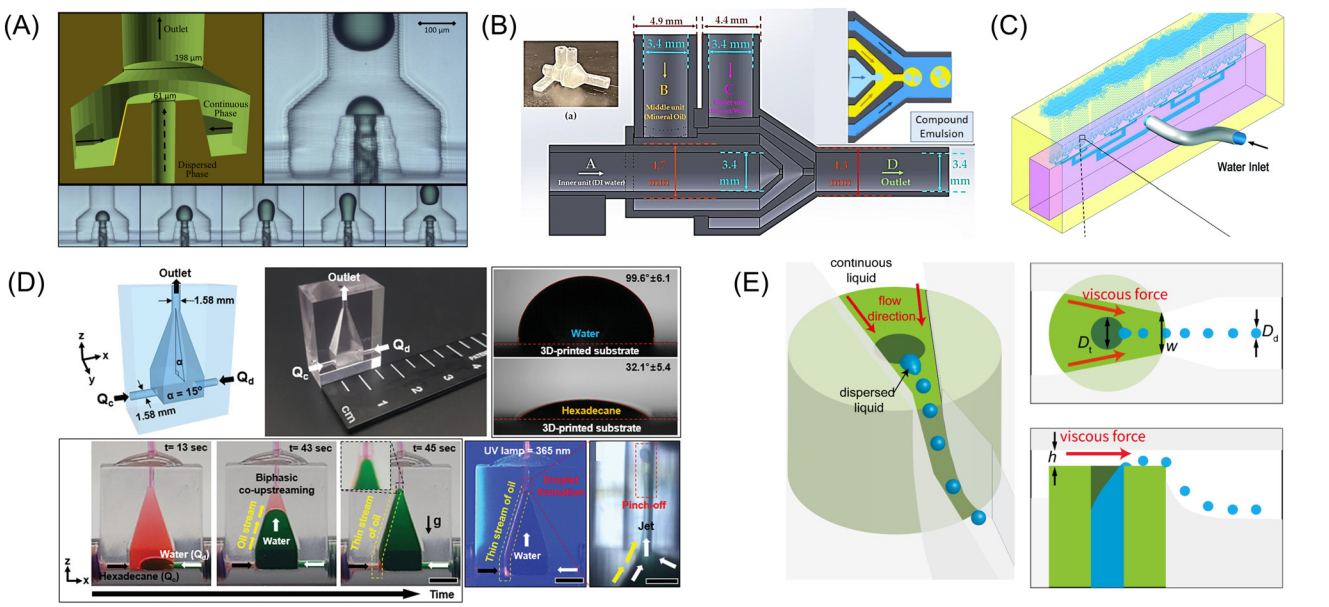

Fig. 3 Representative examples of conventional and advanced 3D-printed droplet generators. A) T-junction and flow-focusing devices prepared by fused filament fabrication. This figure has been adapted from ref. 131 under the Creative Commons Attribution License (CC BY 4.0). B) Axisymmetric co-flow device printed monolithically. This figure has been adapted from ref. 179 under the Creative Commons Attribution License (CC BY 4.0). C) Step emulsifier geometry relying on capillary instabilities at sudden channel expansions. This figure has been adapted from ref. 185 with permission from Royal Society of Chemistry, Copyright 2018. D) Chimney-shaped milli-fluidic device with a vertical outlet. This figure has been adapted from ref. 186 with permission from John Wiley and Sons, Copyright 2019. E) Tip-mode asymmetric hydrodynamic focusing design. This figure has been adapted from ref. 187 with permission from Elsevier, Copyright 2025.

rather than simply copying planar motifs. To achieve robust droplet formation across wide flow-rate windows at millifluidic scales, Hwang *et al.* introduced a chimney-shaped device that uses a tapered void chamber with a vertical outlet, harnessing gravity and density differences to stabilize biphasic focusing (Fig. 3D).[186] To address the issue associated with highly viscous droplet generation, Zhang *et al.* reported a tip-mode system based on three-dimensional asymmetric hydrodynamic focusing. Their printed structure formed a stable liquid tip that was significantly smaller than the physical nozzle outlet. Droplets emitted from this fine tip enabled stable generation of droplets comprising fluids with viscosity up to approximately 300 mPa s, with diameters much smaller than the device's nozzle dimension (Fig. 3E).[187] Overall, these examples mark a transition from using 3D printing as a simple replication tool to employing it as an enabling technology for novel, high-performance droplet generators that were unachievable using conventional methodologies.

4.2. Modular and monolithic routes to scale

Scaling droplet production beyond a single droplet generator requires architectures that preserve uniform flow distribution across many parallel units while remaining easy to assemble, service, and reconfigure. Stacked lithographic chips or manually assembled glass capillaries have demonstrated this at a proof-of-concept level, yet they are labor intensive, alignment sensitive, and difficult to reproduce. 3D printing addresses these limitations by enabling both modular plug-and-play systems and monolithic manifold integration.

A promising strategy is the creation of modular, plug-and-play building blocks that can be connected, disconnected, and reconfigured without specialized tools. Bhargava *et al.* introduced discrete microfluidic elements with standardized cubic footprints and connectors, analogous to Lego bricks, allowing predictable 3D circuits that can be analyzed with network methods (Fig. 4A).[188] Building on this concept, Song *et al.* and Ji *et al.* developed interlocking modules that use cylindrical posts, locking bumps, and snap-fit joints that engage matching grooves on adjoining parts.[19,189] To ensure robust, leak-free seals under operating pressure, these connectors commonly incorporate O-rings seated in machined or printed glands within the female port; axial compression upon mating seals potential leak paths and supports operation to roughly 40 kPa (Fig. 4B). In a complementary approach, Morimoto *et al.* used precision screw threads to produce durable, re-usable couplings suitable for long-term operation and convenient disassembly for cleaning.[190] Hybridization with commercial fittings further extends versatility. Zhang *et al.* printed bodies with integrated threads that mate to standard finger-tight connectors; a replaceable segment of commercial tubing then serves as the nozzle, combining the surface quality and

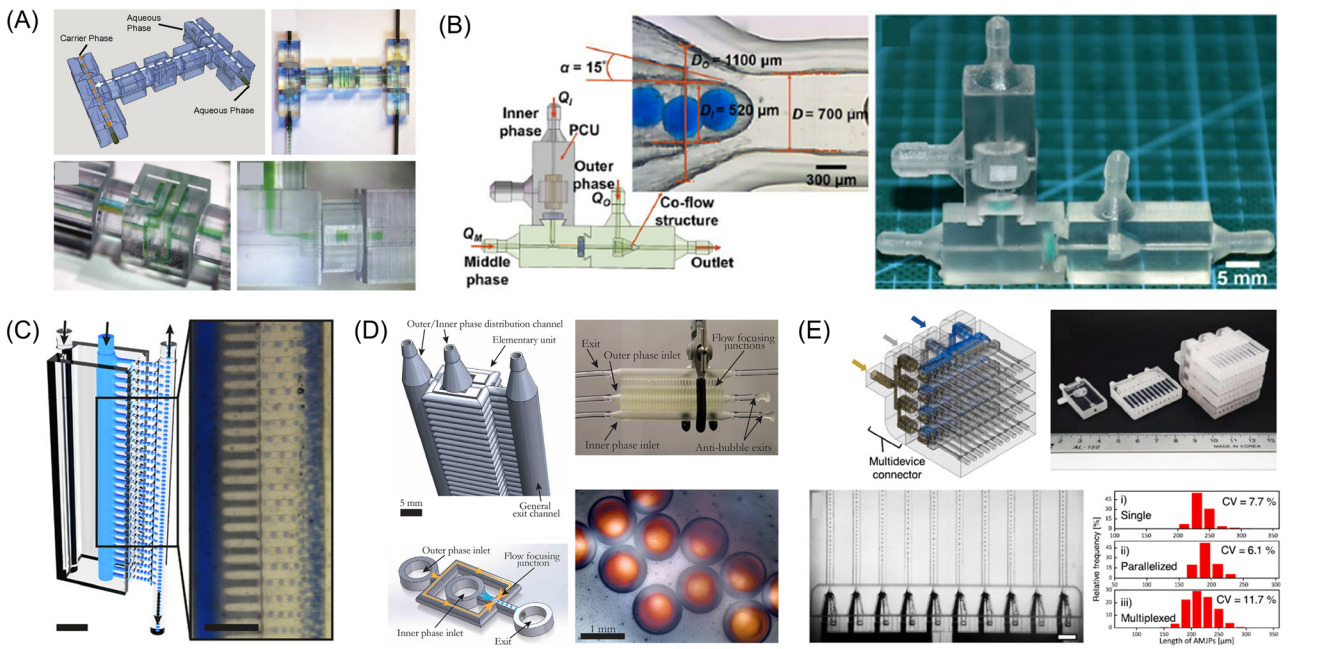

Fig. 4 Representative examples of modular and scalable 3D-printed microfluidic devices for high-throughput droplet generation. A) Modular plug-and-play microfluidic elements with standardized cubic footprints and connectors. This figure has been reproduced from ref. 188 with permission from National Academy of Sciences, Copyright 2014. B) Modular device for double emulsion generation fabricated *via* multimaterial 3D printing, consisting of interchangeable functions. This figure has been adapted from ref. 19 under the Creative Commons Attribution License (CC BY 4.0). C) Monolithic integration of parallel flow-focusing droplet makers into vertically stacked architectures. This figure has been reproduced from ref. 194 with permission from American Chemical Society, Copyright 2015. D) High-throughput monolithic device containing 32 parallel flow-focusing junctions. This figure has been adapted from ref. 195 with permission from Emerald Publishing, Copyright 2021. E) Multiplexed 3D-printed Janus droplet generators for mass production. This figure has been adapted from ref. 168 with permission from Elsevier, Copyright 2023.

dimensional precision of off-the-shelf components with the geometric flexibility of printed housings.[191]

A complementary strategy targets maximum generator density *via* monolithic embedded manifolds. Here, the primary advantage of 3D printing is exploited to embed complex, 3D distribution networks in a single body. Hierarchical, tree-like manifolds are dimensioned to equalize hydraulic resistance to each droplet generator, using design rules analogous to resistor-network optimization, matched path lengths, or deliberate choke channels near each inlet to mitigate maldistribution.[192] In this context, Zhang *et al.* integrated five co-flow generators in one high-resolution micro-printed device.[193] Pushing density further, Femmer *et al.* stacked 28 flow-focusing junctions vertically and fed them with internal distribution channels, reducing footprint and dead volume while maintaining uniform supply (Fig. 4C).[194] At larger scale, Mottin *et al.* realized 32 parallel flow-focusing junctions that produced approximately 14 L per day of monodisperse emulsions and validated the platform by synthesizing magnetic PEG hydrogel beads (Fig. 4D).[195] Throughput gains have also translated into continuous production of advanced materials. Shin *et al.* vertically stacked four 10-nozzle modules to achieve an effective 40-fold increase in production rate for magnetic Janus particles used in oil remediation (Fig. 4E).[168] Functional elements can also be co-printed with the manifolds. Vigogne *et al.* integrated sequential droplet-splitting cascades on the same chip to refine final particle size while sustaining high production numbers.[169]

Overall, 3D printing supports two complementary routes to scale. Modular architectures maximize flexibility, serviceability, and rapid iteration, which is ideal for research and development where devices are frequently reconfigured. Monolithic manifold integration sacrifices some reconfigurability in exchange for maximum nozzle density, compact footprints, and robust distribution, which is advantageous for high-throughput manufacturing. Selecting between these approaches, or combining them within a hybrid system, depends on priorities for flexibility, pressure rating, chemical compatibility, cleaning workflow, and the required production rate.

4.3. Scale-up challenges and failure modes

Despite advances in modularization and manifold integration, scaling a single droplet generator to high channel counts remains difficult primarily due to degradation of droplet monodispersity under parallel operation as the precision of one junction depends on a delicate balance among pressure, interfacial tension, and confinement. As nozzle count rises, small and unavoidable variations in local hydraulic resistance, surface wettability, surfactant adsorption, and geometric tolerances accumulate and translate into measurable size drift across the array. Maintaining identical hydrodynamic conditions at hundreds to thousands of outlets therefore becomes an increasingly complex systems problem.

A central driver of this drift is flow maldistribution induced by pressure drops along the supply manifold. As analyzed by Romanowsky *et al.*, a parallelized chip can be modeled as a hydraulic resistor network. In ladder-type manifolds typical of soft lithography, the feeder channels that deliver fluid to each junction carry non-negligible resistance, which creates a longitudinal pressure gradient. Upstream nozzles experience higher flow rates than downstream ones, and the resulting imbalance directly widens the size distribution. Romanowsky and colleagues reported that the CV increased from below 0.5% in a single unit to >5% in a 15-unit array.[196] Deformation of compliant materials such as PDMS under the elevated pressures required for large arrays further perturbs channel cross-sections and alters resistance in ways that are difficult to predict or control.[197]

To mitigate these undesirable effects, several groups have devised hydraulically balanced distribution networks. Theoretical frameworks by Deng *et al.* and Zhang *et al.* provide design rules for hierarchical or tree-like manifolds that equalize the total resistance from a central inlet to every nozzle.[162,198] Examples include backstepping microflow analysis and gradually varying resistance, which prescribe precise channel widths and lengths to compensate for pressure losses.[162] While such optimization improves uniformity, it often increases device complexity and footprint. In conventional soft lithography, fabricating multi-layer networks with tight layer-to-layer alignment and robust bonding is challenging and can become a dominant failure mode. Thus, scaling requires an integrated strategy that (i) makes the unit cell hydraulically dominant by adding local resistors or inlet chokes so that $R_{\mathrm{unit}} \gg R_{\mathrm{manifold}}$, which desensitizes branch flows to longitudinal pressure gradients, (ii) standardizes interfacial chemistry across all nozzles *via* durable coatings and tightly controlled surfactant protocols to prevent wetting-induced regime drift, (iii) increases structural stiffness and manages pressure using rigid substrates or high-modulus printed resins, short unsupported spans, and back-pressure regulation, (iv) tightens geometric tolerances with metrology-informed design margins and calibration coupons that reproduce the smallest vias and throats, and (v) embeds simple diagnostics such as inline pressure taps, optical readouts, or flow sensors to detect maldistribution early and enable correction. With coherent hydraulic design, uniform surface chemistry, and mechanically robust layouts, large arrays can sustain the droplet monodispersity that underpins the value of droplet microfluidics.

4.4. Volumetric manifolds for uniform distribution

The fundamental limitations of planar fabrication in flow distribution and assembly complexity can be overcome by

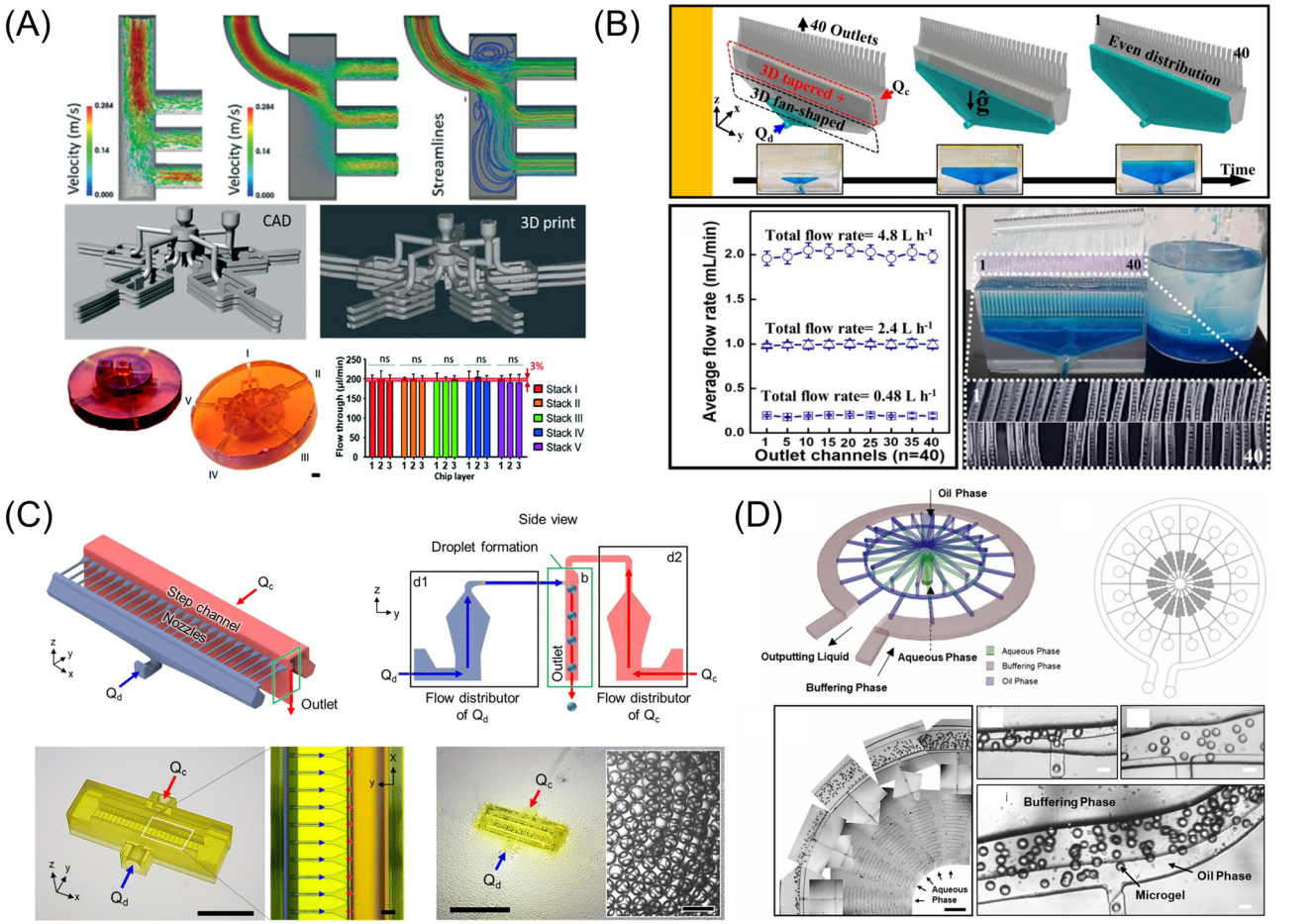

Fig. 5 Representative examples of volumetric and embedded manifold designs enabled by 3D printing for uniform flow distribution and scalable droplet generation. A) CFD-guided design of stacked and radially multiplexed microflow distributors. This figure has been adapted from ref. 174 with permission from Royal Society of Chemistry, Copyright 2020. B) Fan-shaped and tree-like distributor designs integrated into devices with up to 40 outlets. This figure has been adapted from ref. 177 with permission from Elsevier, Copyright 2022. C) Embedded 3D distributor structures with hydrodynamically optimized branching channels that ensure uniform droplet formation across multiple outlets, validated by both simulations and experiments. This figure has been reproduced from ref. 176 with permission from Royal Society of Chemistry, Copyright 2024. D) Radially symmetric distribution manifolds fabricated as monolithic parts. This figure has been adapted from ref. 199 with permission from IOP Publishing, Copyright 2022.

exploiting the volumetric design freedom of 3D printing, which enables internal, multi-layered manifolds and non-planar channel architectures that cannot be realized by glass capillary assembly or conventional soft lithography. By printing monolithic devices that integrate hydrodynamically optimized bifurcations and distributors, designers can replace ladder-type feeders that suffer from longitudinal pressure gradients with compact, symmetric networks that equalize inlet-to-nozzle hydraulic resistance across large arrays. Computational fluid dynamics (CFD) simulation has been used as a forward design tool in this context, as in the work of Kamperman *et al.*, where simulations guided a stacked and radially multiplexed distributor whose printed embodiment reduced nozzle-to-nozzle flow variation to less than 3% relative to non-optimized layouts (Fig. 5A).[174] Related strategies by Hwang *et al.* implemented a three-dimensional fan-shaped distributor with a tapered guider to deliver uniform flow to 40 parallel nozzles for robust droplet formation (Fig. 5B)[177] and later adapted a similar volumetric manifold to a gravity-assisted step emulsification platform with 24 parallel nozzles for high-viscosity formulations (Fig. 5C).[176] Crucially, these designs are fabricated as single, continuous parts, which eliminates manual layer alignment and post-bonding steps that dominate failure modes in stacked-chip approaches as layer count rises. The integrated methodology scales further, as demonstrated by Zhang *et al.* in large-scale single-cell encapsulation, where a radially parallelized distribution network apportioned fluids evenly from a single inlet to as many as 80 droplet generators (Fig. 5D).[199] Collectively, direct embedding of hydrodynamically efficient distributors within monolithic 3D-printed bodies provides a practical pathway to high-throughput parallelization with preserved monodispersity, while simultaneously improving reliability, reproducibility, and

manufacturability beyond what is feasible with conventional planar fabrication methods.

4.5. Applications enabled by scalable generators

The scalability of 3D-printed devices, enabled by integrated manifold architectures and volumetric channel networks, has advanced droplet generation from a low-throughput laboratory technique to a practical platform for the mass production of functional materials. Liter-per-day production has been demonstrated for diverse emulsion-templated particles, including biodegradable polycaprolactone (PCL) microspheres, poly(ethylene glycol) (PEG) microgels, and amphiphilic magnetic Janus particles for environmental remediation.[168,177] These examples indicate that 3D-printed platforms can bridge bench-scale development to application-relevant throughputs while maintaining monodispersity and formulation control.

The capacity to mass-produce monodisperse single emulsions on 3D-printed platforms provides a feasible route to scale many applications originally demonstrated with soft lithography or glass capillaries. As these applications rely on simple single-emulsion templates, they are well matched to parallelizable, monolithic 3D-printed generators that can enhance accessibility and output. In therapeutic particle synthesis, for example, single droplets act as uniform microreactors for polymer microspheres with finely tuned properties that are difficult to achieve in bulk.[200–202] Wei *et al.* used a droplet platform to study solidification kinetics and showed that amorphous polymers can entrap drugs more effectively than crystalline analogs, which motivated a random copolymer that increased the indomethacin loading degree by more than 20-fold (Fig. 6A).[203] Beyond templating, Pires *et al.* leveraged droplets as isolated reactors for high-throughput Layer-by-Layer (LbL) assembly of polyelectrolyte nanoparticles, achieving precise control over size and shell composition for advanced drug delivery vehicles (Fig. 6B).[204] In analytical separations, Sun *et al.* manufactured highly monodisperse porous microspheres as chromatographic stationary phases, where uniform particle size and internal porosity minimized band broadening and improved column efficiency (Fig. 6C).[205]

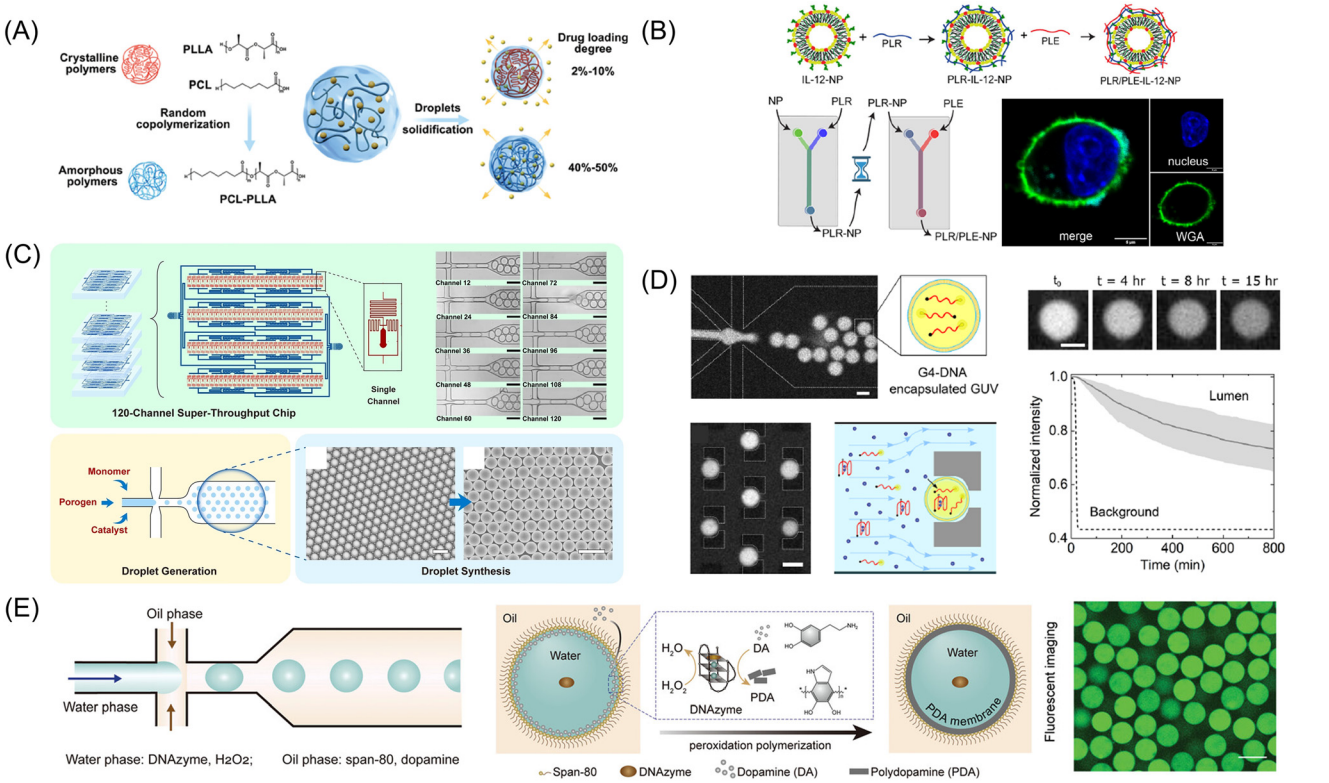

Fig. 6 Representative applications of single emulsion templates for the synthesis of functional microparticles and artificial cell models. A) Drug-loaded polymeric microspheres produced from emulsion droplets. This figure has been adapted from ref. 203 with permission from John Wiley and Sons, Copyright 2025. B) Layer-by-Layer (LbL) assembly using single emulsions as isolated microreactors for sequential polyelectrolyte deposition. This figure has been adapted from ref. 204 under the Creative Commons Attribution License (CC BY 4.0). C) High-throughput microfluidic synthesis of porous polymer microspheres for use as stationary phases in HPLC. This figure has been reproduced from ref. 205 with permission from John Wiley and Sons, Copyright 2025. D) Giant unilamellar vesicles (GUVs) generated from single emulsions and used as artificial cell models to encapsulate DNA-based fluorescent probes for the optical quantification of ion transport across membranes. This figure has been adapted from ref. 209 under the Creative Commons Attribution License (CC BY 4.0). E) Polydopamine (PDA) capsules fabricated *via* interfacial polymerization at the droplet interface, serving as robust protocell models with semi-permeability and photothermal conversion capability for biochemical mimicry. This figure has been adapted from ref. 210 with permission from John Wiley and Sons, Copyright 2025.

Single emulsions also underpin model systems in biophysics and synthetic biology.[206–208] Fletcher *et al.* generated giant unilamellar vesicles from single-emulsion templates and employed them as picoliter microreactors to encapsulate a DNA-based fluorescent sensor, enabling direct optical quantification of potassium transport across lipid membranes (Fig. 6D).[209] Using W/O emulsion droplets as templates, Hu *et al.* formed uniform polydopamine capsules through interfacial polymerization, yielding robust protocell models with size-dependent semi-permeability and strong photothermal response that can trigger internal biochemical reactions (Fig. 6E).[210] Given that 3D printing can now mass-produce the underlying single-emulsion templates, these and related use cases in materials synthesis, biophysical analysis, and diagnostics are well positioned to benefit from 3D-printed, high-throughput devices that combine design flexibility with reproducible, industrially relevant output.

5. Wettability programming for double and higher-order emulsions in 3D-printed devices

Based on these architectural and scale-up strategies, the next lever for moving beyond single emulsions in 3D-printed microfluidics is stable, spatially programmed wettability inside printed channels. As-printed photopolymers are typically moderately hydrophobic and chemically heterogeneous, which narrows the dripping window. Locking wall–phase affinity and then inverting it at prescribed junctions enables W/O/W and O/W/O double emulsions, Janus droplets, and multi-compartment carriers while keeping monodispersity in parallelized devices. The toolkit spans gas- or UV/ozone activation followed by covalent grafts, barrier layers such as parylene or thin fluoropolymers to suppress leaching, inorganic passivation for durable hydrophilicity, and materials-first or multi-material printing that encodes polarity without post-coats. In cases where enclosed features demand localization, fill-and-drain chemistries, segmented-flow LbL, and inkjet deposition also provide route-specific patterning, and thermo-responsive grafts offer reversible switching. With these methods in place, double emulsions translate directly to high-throughput bioassays, protocell and giant unilamellar vesicles (GUV) platforms, programmable microreactors, hierarchical materials, responsive delivery systems and beyond.

5.1. Surface modification techniques for 3D-printed microchannels

Stable droplet generation in 3D-printed devices requires fixing the channel wall's affinity to the intended continuous phase and maintaining that state under sustained, surfactant-containing flows. As-printed microchannels prepared from photopolymer resins are typically moderately hydrophobic and chemically heterogeneous after wash and post-cure, and they may leach low-molar-mass species that perturb interfacial tension and wetting behavior. These factors compress the usable dripping window at finite Ca, shift the O/W to W/O switching threshold, and can degrade droplet monodispersity unless CAH and fouling are controlled beyond what is captured by nominal static contact angles; therefore, wettability stability should be assessed using dynamic metrics such as advancing and receding contact angles and the resulting contact angle hysteresis, rather than static contact angles alone. In parallelized or long-manifold architectures with enclosed features, spatial uniformity of the surface state is therefore a central design constraint. Treatments are best evaluated on durability, reproducibility, and scalability inside sealed channels rather than on initial contact angles alone.[144,177,186]

Gas-phase activation can prime hydrophilicity but the effect is typically not permanent. Emde *et al.* demonstrated on commercial SLA (meth)acrylate resins that brief O_2 plasma lowers water contact angle, although stability is often transient in practice.[211] UV or ozone activation shows similar storage-dependent retention of hydrophilicity and surface free energy in which the activation-induced wetting states often relax on timescales of hours to days due to hydrophobic recovery, particularly under humid environments or surfactant-containing flows.[212,213] Since such activation methods are line-of-sight and prone to hydrophobic recovery, it is most effective as a primer to be followed immediately by covalent or barrier stabilization. We note that robust solution-phase silanization on certain (meth)acrylate prints can proceed without plasma pre-oxidation.[69]

Covalent grafting provides durable control of surface energy and hysteresis. Bacha *et al.* used benzophenone-sensitized UV grafting to photochemically deposit a thin methacrylate layer inside SLA-printed channels, reducing water contact angle from about 97° to about 25°, enabling stable production of O/W emulsions without altering the bulk mechanics.[68] Azim *et al.* employed mussel-inspired polydopamine as a pragmatic primer, where brief corona activation followed by alkaline dopamine deposition lowered water contact angle to about 35–45° and increased the corresponding surface free energy to about 60 mJ m^{-2} in DLP resins.[214] The resulting catechol and amine functionalities then enabled secondary grafting to impart either hydrophilic or hydrophobic character. These liquid-phase approaches can also modulate contact-angle hysteresis and improve resistance to aging-induced wettability drift during extended operation. In addition, they are compatible with post-cured parts, support spatial patterning, and allow tuning of surface polarity and hysteresis to match the desired emulsion mode.

Hydrophobic operation can be stabilized by fluorinated silanes and thin fluoropolymer skins. Catterton *et al.* reported solution-phase fluoro-silanization on (meth)acrylate prints that achieved water contact angles above 110° with low hysteresis *via* a simple dip-and-rinse from a fluorinated carrier (Fig. 7A).[69] They established covalent monolayers confirmed through attenuated total reflectanc-Fourier transform infrared spectroscopy (ATR-FTIR) analysis,

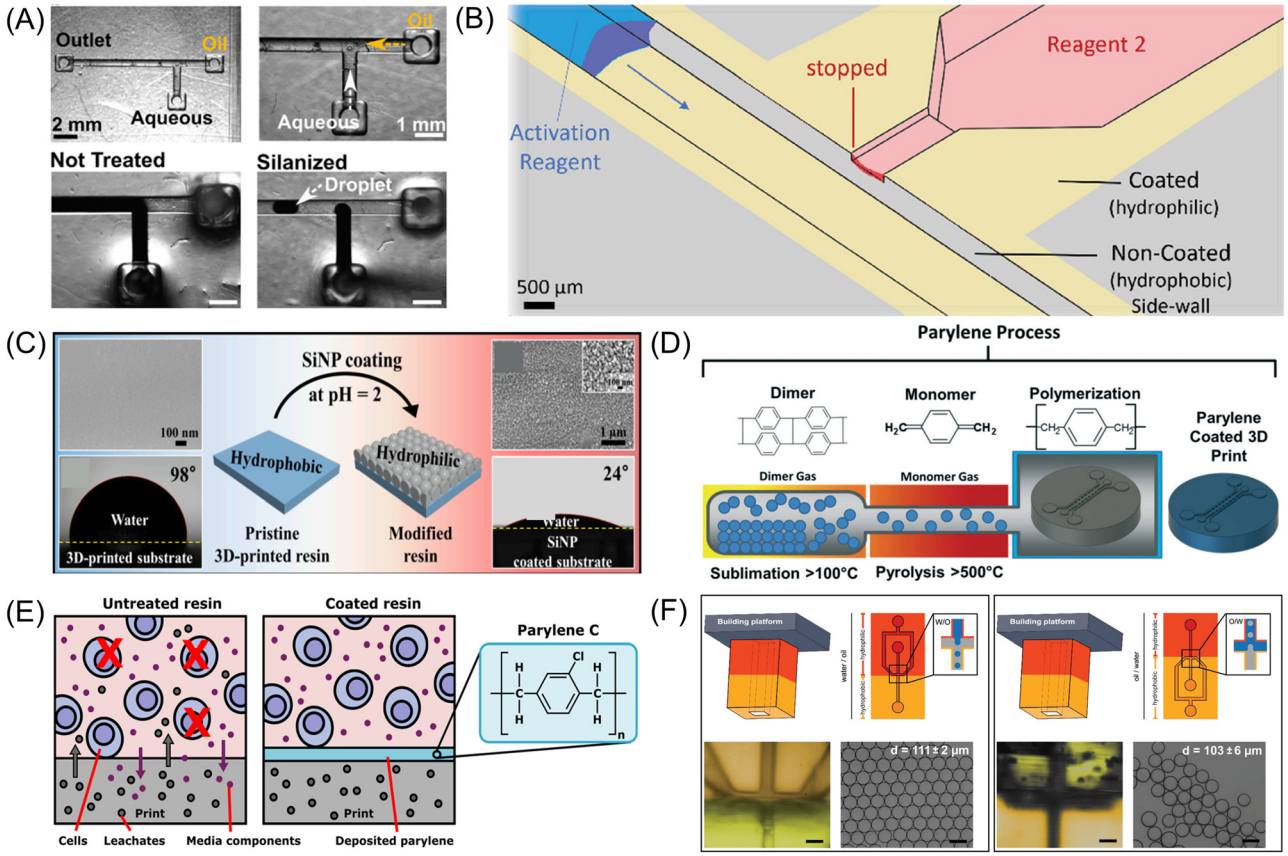

Fig. 7 Representative surface modification techniques applied to 3D-printed microfluidic devices. A) Fluorosilane treatment enabling droplet generation in SLA-printed T-junction channels. This figure has been reproduced from ref. 69 with permission from American Chemical Society, Copyright 2021. B) Inkjet-printed hydrophilic coatings for capillary-driven flow control. This figure has been adapted from ref. 72 under the Creative Commons Attribution License (CC BY 4.0). C) Silica nanoparticle coating for hydrophilic modification and O/W emulsion formation. This figure has been adapted from ref. 177 with permission from Elsevier, Copyright 2022. D) Parylene coating on SLA prints to enhance biocompatibility and enable PDMS molding. This figure has been reproduced from ref. 130 with permission from Royal Society of Chemistry, Copyright 2021. E) Parylene-C coating as a protective barrier against leaching and erosion in resin-based devices. This figure has been reproduced from ref. 129 with permission from American Chemical Society, Copyright 2023. F) Multi-material printing with hydrophilic–hydrophobic resin patterning for emulsion generation. This figure has been reproduced from ref. 216 under the Creative Commons Attribution License (CC BY 4.0).

patterned open surfaces by masking, and functionalized enclosed channels by fill-and-drain, resulting in performance that retained even after abrasion, solvent exposure, and storage. The retention of low CAH after mechanical, chemical, and storage stress highlights the importance of assessing wettability stability under extreme and application-relevant conditions, rather than at a single time point. These conditions suit W/O dripping and passive capillary barriers, and the ability to pattern wetting in both open and enclosed regions is attractive for multiphase control. We also note that as solution-borne chemistries remain sensitive to solvent pathways and environmental humidity, reporting hysteresis and stability under surfactant load and thermal cycling is often useful.

Moreover, solvent–resin interactions and humidity should be also managed to limit swelling, and aging or flow-history effects should be reported alongside advancing and receding angles.[144]

As a complementary route to spatial control, Makhinia *et al.* inkjet-printed hydrophilic patches on 3D-printed substrates to steer local flow, illustrating patternable, on-demand wettability even in open structures (Fig. 7B).[72]

An inorganic passivation layer can also impart robust hydrophilicity and solvent resistance. Hwang *et al.* immobilized a conformal SiO_2 layer inside SLA channels using acidified colloidal silica, lowering water contact angle from about 98° to about 24° and retaining hydrophilicity under organic-solvent exposure (Fig. 7C).[176,177] We note that although this subsection emphasizes enclosed channels, the same palette translates to open-surface digital microfluidics where mixed wettability is exploited rather than eliminated. Kanitthamniyom *et al.* combined a Teflon-AF hydrophobic background that reduces friction and suppresses spreading with polydopamine-defined surface-energy traps as local hydrophilic anchors on a printed, modular platform, enabling precise droplet anchoring and on-chip aliquoting or serial dilution *via* controlled necking. They also demonstrated passive mixing with textured, Teflon-coated pillars that used controlled Wenzel adhesion

to induce a sling-type rebound and rapid homogenization.[215]

In addition, barrier coatings suppress leaching and stabilize wetting over long operation. O'Grady *et al.* deposited conformal parylene-C from the vapor phase to create pinhole-free diffusion barriers that stabilized low-hysteresis wetting and blocked leachables from printed acrylates (Fig. 7D),[130] with subsequent studies demonstrating cytocompatibility and reduced small-molecule uptake under repeated 37 °C perfusion (Fig. 7E).[129] These results emphasize that long-term wettability stability is operationally defined by sustained device performance over hours to weeks, rather than by initial surface characterization alone. When ultra-low surface energy is required, thin fluoropolymer films provide clear, low-hysteresis interfaces for droplet manipulation and imaging. In printed contexts, dilute solution coatings such as Teflon-AF by dip or spin are most reliable for enclosed channels, while vapor-deposited options are generally limited to open structures.[144]

Material choice and multi-material printing can encode wetting without secondary coatings. Männel *et al.* employed multi-material printing to program spatial wetting sequences, hydrophobic to hydrophilic to hydrophobic, stabilizing O/W/O double emulsions in planar junctions (Fig. 7F).[216] This materials-first approach complements studies showing that intrinsically hydrophilic resins printed as cylindrical SLA channels can support reliable O/W formation in co-flow devices without additional surface modulation, and it is consistent with broader surveys of wettability strategies in 3D-printed microfluidics.[131] In practice, robust workflows integrate material selection, geometry, and surface modification to operate within a stable regime while minimizing aging- and history-induced wettability drift during long-term and parallelized operation.

5.2. Spatial wettability programming for complex emulsions

One practical way to implement spatial wettability programming is local chemical patterning after full post-cure. A representative case is masked fluoro-silanization on SLA or DLP acrylates where an adhesive mask protects non-target regions while a dilute fluorosilane bath modifies only the intended segment. This creates hydrophobic patches on otherwise untreated prints and the same chemistry reaches enclosed features by fill and drain while preserving channel geometry. Selective fluorination converts a printed T-junction into the W/O regime whereas the unmodified device wicks the aqueous phase. On open facets, a hydrophobic patch acts as a surface tension barrier that compartmentalizes fluids.[69] The idea also extends to digital deposition. Inkjet-printed hydrophilic pixels based on a PSS-Na formulation can be written onto targeted regions of multilevel printed channels so that capillary stop or delay elements and priming stripes appear exactly where aqueous streams should start cleanly. The patterned wetting persists after storage and is used to route liquids to an embedded, fully printed OECT chloride sensor. While this study focuses on programmed delivery rather than dispersed phase droplet generation, it demonstrates robust selective wetting control in devices that can be replicated across manifolds.[72]

An orthogonal route embeds the pattern during fabrication. In a materials-first variant, intrinsically hydrophilic and hydrophobic projection microstereolithography resins are alternated within a single build, hard-coding the wettability sequence at the voxel scale. A PEGDA or acrylic acid formulation prints hydrophilic regions and a fluorinated acrylate prints hydrophobic counterparts. Vats are swapped at the layer or voxel level to lay down hydrophobic to hydrophilic to hydrophobic sequences across consecutive junctions in planar chips. Practical constraints are handled in process, so transitions remain sharp at junctions where regime switching is needed. The built-in sequences support W/O and O/W single emulsion droplets and importantly, a planar O/W/O double emulsion generator without any post-coating step.[216]

Mixed wettability on open printed platforms can supply or complement enclosed droplet stages. In a modular, magnetically actuated digital microfluidic architecture, a Teflon AF background provides low-friction transport, while polydopamine surface-energy traps furnish localized anchoring at predefined pads. Magnetic particle-laden droplets shuttle between transport and anchor zones to perform dispensing, merging, aliquoting, particle extraction, and mixing. These operations have enabled immunoassays, pathogen identification with susceptibility testing, and enzymatic sensing by manipulating discrete droplets on pattern printed substrates. Although droplets are manipulated rather than emulsified at these sites, the same design vocabulary, hydrophobic regions for transit and localized hydrophilic sites for capture, translates directly to hybrid printed systems that precondition small volumes upstream of enclosed emulsifiers.[215]

Although reports on fully 3D-printed architectures are still limited, extensive work in planar PDMS and glass-capillary platforms has established the necessity of selective wettability patterning. In PDMS devices, spatially resolved surface modification, combining localized oxidation with protected or re-hydrophobized regions, sets the first junction hydrophobic for W/O and the second hydrophilic for O/W, enabling W/O/W or O/W/O double emulsions in sequence; the approach scales to arrays of generators (Fig. 8A and C).[48,217,218] LbL assembly of polyelectrolytes driven by syringe-vacuum segmented flow extends selective patterning to nonplanar PDMS geometries, rapidly writing hydrophilic and hydrophobic segments along the flow path and supporting double and even triple emulsions in multi-junction chips (Fig. 8B).[49] Rapid, low-cost spatial patterning in PDMS has likewise yielded continuous production of monodisperse double emulsions after simple in-chip treatments, demonstrating that the programmed sequence of wall affinities rather than any single chemistry is the primary design variable (Fig. 8D).[219] Alignment-free

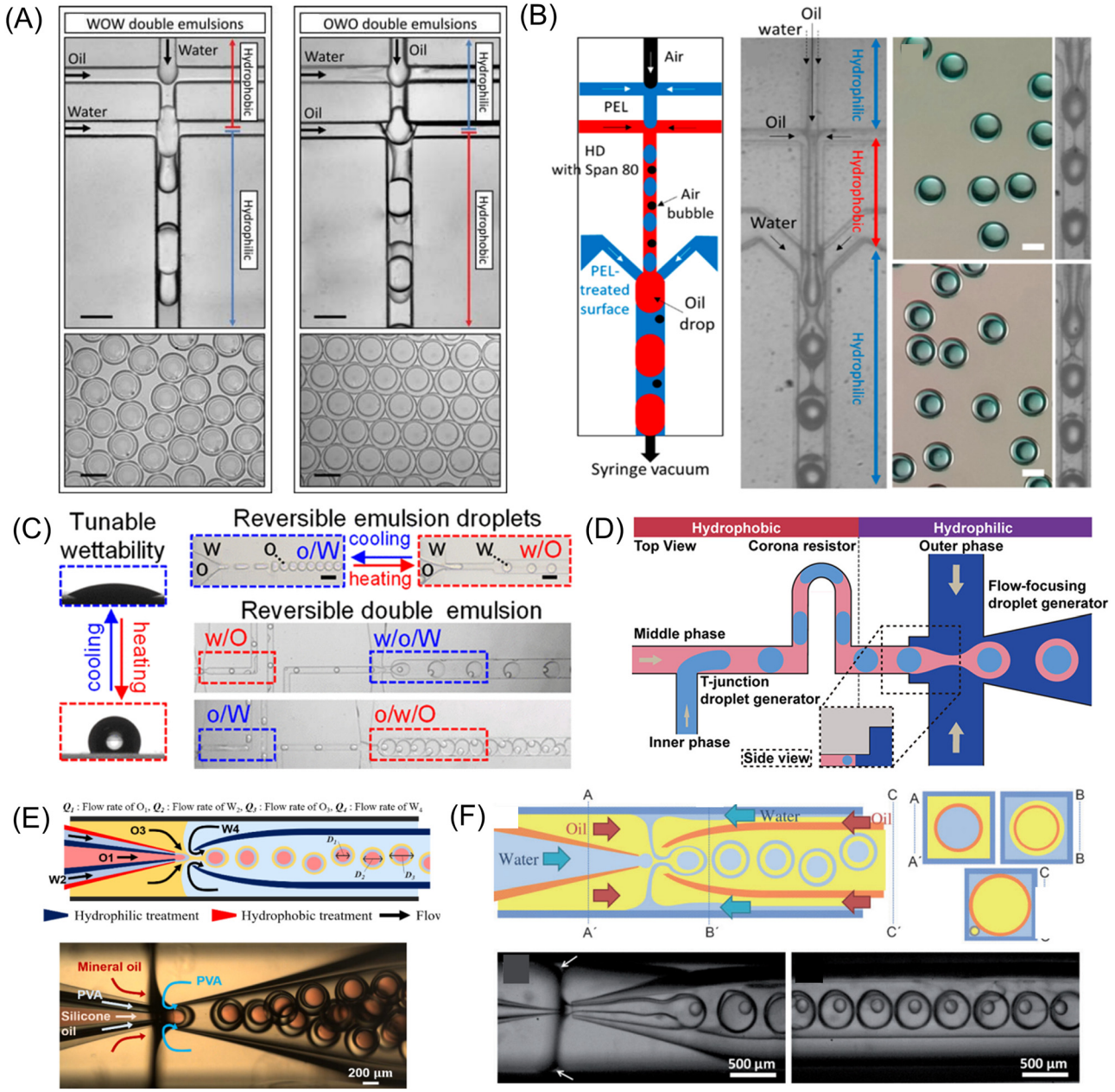

Fig. 8 Representative wettability patterning strategies for 3D-printed microfluidic droplet generators. A) Flow-confinement-based patterning enabling hydrophilic–hydrophobic transitions for W/O/W and O/W/O emulsions. This figure has been reproduced from ref. 217 with permission from Royal Society of Chemistry, Copyright 2010. B) Layer-by-Layer polyelectrolyte deposition guided by segmented flow for selective modification in nonplanar devices. This figure has been adapted from ref. 49 with permission from American Chemical Society, Copyright 2018. C) Thermoresponsive PNIPAAm-grafted channels for reversible wettability switching and multiform emulsion generation. This figure has been adapted from ref. 218 with permission from American Chemical Society, Copyright 2019. D) Localized corona discharge for spatial wettability patterning to generate monodisperse W/O/W emulsions. This figure has been adapted from ref. 219 with permission from American Chemical Society, Copyright 2021. E) Selective hydrophilic/hydrophobic modification of concentric capillaries for stable W/O/W emulsions. This figure has been adapted from ref. 10 with permission from American Chemical Society, Copyright 2024. F) One-step emulsification of multiple concentric shells using capillary devices with opposite wall modifications. This figure has been reproduced from ref. 221 with permission from John Wiley and Sons, Copyright 2010.

constructions that embed wettability contrast further demonstrate reliable W/O/W formation without delicate multi-part registration, a consideration directly relevant when long printed manifolds must repeat the same orchestration at scale (Fig. 8E and F).[10,220,221] In coaxial glass-capillary devices, pairing a hydrophobic inner generator with a hydrophilic encapsulator in series produces monodisperse double emulsions and sets a canonical standard for decoupling inner and outer droplet sizes, highlighting how strictly the surface sequence must be

achieved.[158] For Janus outcomes, region-selective modification along the wetted path has produced water–oil Janus droplets and, after curing, hydrophilic–hydrophobic anisotropic microparticles, providing a clear precedent for wettability patterning as a design variable beyond core–shell double emulsions.[222]

These selective tools translate directly to printed implementations for structured droplets. Standardized module libraries produced by microstereolithography enable side-by-side Janus streams and controlled coalescence or merging before shell formation, offering plug-and-play routes to structured droplets within the same printed stack.[105] In separate modular demonstrations, multimaterial printed devices create single and double emulsions by assigning surface preference module-by-module; for example, with a hydrophobic T-junction upstream and a hydrophilic co-flow downstream.[19] Downstream transport studies clarify why the wall-affinity sequence must remain intact. When Janus droplets encounter bifurcations or secondary necks, breakup modes and size symmetry depend on confinement and the local wall–phase relation, and operating maps can be defined in terms of Ca and geometry.[48]

Looking ahead, methods that confine or tune wettability only within targeted segments of enclosed printed channels remain limited in spatial precision, chemical breadth, and throughput. Progress in these selective wettability approaches, together with advances in digital deposition, resin-level polarity programming, and hybrid chaining of open and enclosed stages, would establish wettability programming as a general design variable. Such developments are expected to enable routine generation of double emulsions and Janus droplets with predictable operating windows and improved tolerance to prolonged or high-stress operation across printed architectures, thereby facilitating translation to anisotropic particle fabrication. Despite the increasing use of dynamic wetting metrics, device-level stability criteria, and stress-based evaluations, current assessment practices remain highly heterogeneous. Different studies adopt distinct definitions of wettability stability, time horizons, and failure modes tailored to specific materials and operating conditions, rendering quantitative metrics such as CAH, stable operating windows, and time-to-failure difficult to compare across platforms. As no field-wide qualification protocol exists for systematically assessing long-term wettability stability in 3D-printed droplet microfluidic devices, establishing a minimal reporting standard and qualification workflow may therefore provide a critical step toward reliable scale-out, cross-study comparability, and application-driven translation.

5.3. Application fronts enabled by complex emulsions

Multiple and complex emulsions extend droplet microfluidics beyond single-core carriers by introducing nested interfaces that can be independently programmed for transport, reaction, protection, and readout.[223–226] In practice, these capabilities are reliable only when wall–phase interactions are programmed across successive junctions so that the intended continuous phase prewets one segment and the interfacial preference inverts at the next. Collectively, these examples demonstrate that reliable multiple-emulsion generation critically depends on maintaining appropriate wettability contrasts across successive junctions. At the device level, such contrasts are governed by intrinsic surface chemistry, material selection, and the operational stability of surface modifications, rather than by junction geometry alone, consistent with the physicochemical constraints governing droplet formation discussed earlier. With appropriate wettability patterning, double and higher order emulsions are generated with uniform shells that tolerate downstream manipulations. As programmable microreactors, double emulsions enable reagent staging and timed environmental changes that are difficult to implement with single emulsions. Cowell *et al.* showed that reagents can be introduced into double emulsions in a controlled, drop-by-drop manner while preserving droplet identity, effectively turning each capsule into a multistep reaction vessel without rupturing the carrier. The workflow uses transient conversion and re-shelling to add inputs on demand while maintaining encapsulation fidelity throughout the assay.[227] In a complementary example, Rana *et al.* produced W/O/W droplets of approximately 100 to 200 μm with mineral oil shells tunable to about 10 to 40 μm and used an enzyme reaction to generate on-demand base pulses.[228] They demonstrated that diffusion across the oil layer and shell thickness can be used as design dials to steer pH-time trajectories and select among distinct particle formation pathways under otherwise identical bulk conditions. Building on the concept that interfaces can function as regulatory elements for transport and reaction progress, multiplexed cell-free synthesis and functional screening of antimicrobial peptides can be co-localized with reporter vesicles inside double emulsions so that expression and membrane selectivity readouts proceed without crosstalk, followed directly by flow cytometric selection (Fig. 9A).[229]

Living and soft-matter systems likewise benefit from protective yet permeable multi-interface architectures. Isa *et al.* encapsulated GFP-labeled bacteria in microfluidic W/O/W droplets of about 100 μm with inner aqueous cores near 40 to 50 μm and mapped release regimes in which modest osmotic imbalances trigger a two-step destabilization pathway and controlled escape without the whole shell collapsing. They outlined how diffusive and osmotic balances can be tuned to program biological exposure while maintaining compartment integrity.[230] For bottom-up synthetic biology, Bakouei *et al.* introduced a PDMS–glass hybrid capillary platform that forms double emulsions over a wide size range and coupled them to rapid purification to generate giant liposomes.[231] In this system, robust double-emulsion formation is achieved by encoding wettability contrast directly through material selection, using hydrophilic glass and intrinsically hydrophobic PDMS, which

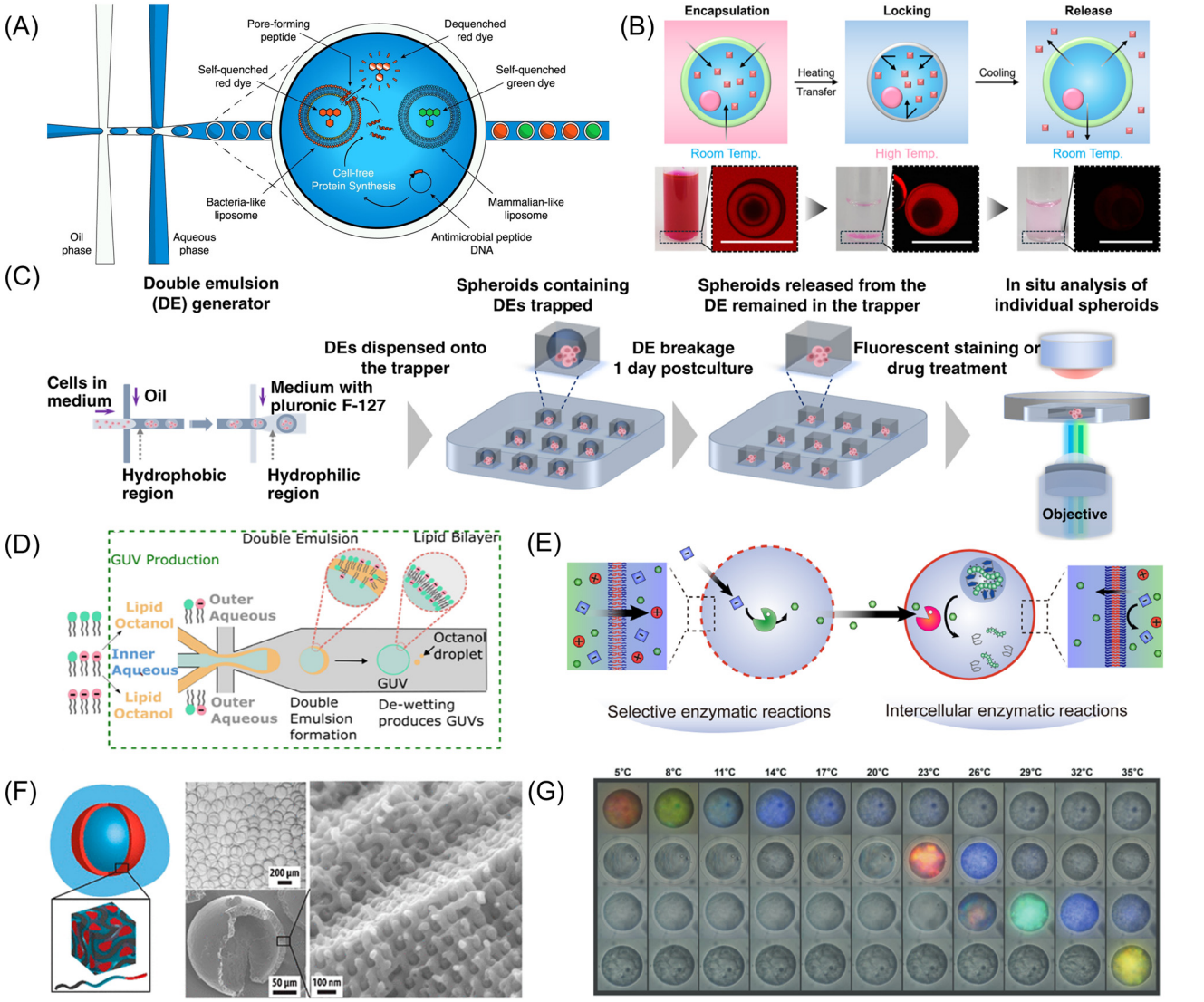

Fig. 9 Multiple emulsion applications enabled by wettability control. A) Cell-free synthesis and high-throughput screening of antimicrobial peptides in double emulsions. This figure has been reproduced from ref. 229 under the Creative Commons Attribution License (CC BY 4.0). B) Thermoresponsive hydrogel microcapsules with phase separation-induced mechanical toughening and programmable release. This figure has been reproduced from ref. 233 under the Creative Commons Attribution License (CC BY 4.0). C) Double emulsion-pretreated microwell culture for uniform spheroid formation and drug testing. This figure has been reproduced from ref. 235 under the Creative Commons Attribution License (CC BY 4.0). D) On-the-fly control of lipid composition in GUVs validated by DNA probes. This figure has been reproduced from ref. 236 under the Creative Commons Attribution License (CC BY 4.0). E) Programmable enzymatic reaction networks in polymersomes for out-of-equilibrium dynamics and communication. This figure has been reproduced from ref. 237 under the Creative Commons Attribution License (CC BY 4.0). F) Ordered mesoporous microcapsules from block copolymer self-assembly in double emulsions. This figure has been reproduced from ref. 238 with permission from American Chemical Society, Copyright 2021. G) Thermochromic microcapsules containing cholesteric mesogens enclosed by alginate hydrogel shells. This figure has been reproduced from ref. 241 with permission from John Wiley and Sons, Copyright 2021.

reduces reliance on post-fabrication surface treatments and enhances operational stability. This material-encoded wettability concept offers a direct analogue for 3D-printed devices, where resin choice and native surface chemistry can similarly predefine wettability contrasts without extensive post-processing. In translational delivery, palm oil shelled double emulsions produced in a flow-focusing glass capillary device hermetically encapsulate otherwise problematic alcohol solvents and high-content actives. They enable debris-free, on-demand release by heating, shear, or photothermal inputs while maintaining skin-compatible composition, which demonstrate how shell material choice and double emulsion geometry can solve compatibility and triggering constraints in transdermal systems (Fig. 9B).[232,233]

For cellular and molecular bioassays, a central practical advantage of double emulsions is compatibility with high-throughput sorting while preserving isolation. Ding *et al.* defined operating conditions for thin-shelled double emulsions that maintain structural integrity and optical readability in standard flow cytometers, enabling multicolor

sorting of encapsulated cellular interaction assays without catastrophic drop failure.[234] In related culture workflows that benefit from a brief but well-controlled complex emulsion step, pre-treating microwells with microfluidic double emulsions initiates uniform multicellular spheroids and supports sustained culture with *in situ* spectroscopic analysis. This illustrates how a transient multi-interface scaffold can standardize an otherwise variable microenvironment (Fig. 9C).[235] Together with the cell-free, multiplex-ready reactors noted above, these developments position double emulsions as assay carriers in which interfaces, rather than bulk exchanges, gate reaction progress and data acquisition.[229]

For biological and synthetic cellular applications, multiple emulsions are increasingly used not only as passive containers but as programmable reaction vessels in which interfaces define communication and reaction boundaries. Fletcher *et al.* established a continuous microfluidic workflow that modulates giant vesicle composition during production and coupled this with immediate, single-vesicle readouts, enabling rapid mapping between membrane makeup and function. By perturbing and quantifying vesicles on the fly rather than in batch, the platform turns complex, multi-interface carriers into screenable assay objects and shortens the iteration cycle for artificial-cell libraries. In the context of double and higher-order emulsions, this shows how compositional control and inline analytics can be fused to program transport and signaling at the compartment level (Fig. 9D).[236] Seo *et al.* created artificial cell-like polymersomes whose selective membrane permeabilities gate substrate exchange into enzyme modules, forming a programmable reaction network that can be reconfigured by external cues (Fig. 9E).[237] By combining compartments with distinct transport properties and coupling them through controlled diffusion, they realized time-ordered transformations that remain isolated from crosstalk yet communicate as designed. The result is a general blueprint for using multi-interface containers to stage and route biocatalysis beyond what single emulsions can reliably support.

Meanwhile, multiple emulsions serve as materials templates, decoupling geometry from mass transfer in ways that single emulsions cannot. Werner *et al.* confined amphiphilic block copolymer self-assembly within the shell of double emulsions to yield polymeric microcapsules with homogeneous, ordered mesopores, thereby programming nanometer-scale permeability independently of capsule size and shape set by the microfluidic geometry (Fig. 9F).[238] In a different class of functional solids, Ma *et al.* exploited the coupling between liquid crystal order and polymer stabilizer adsorption in emulsion shells to template photonic microparticles whose optical textures can be reconfigured before fixation and then locked by polymerization, pointing to responsive labels and miniaturized optical components in which interfacial alignment is a controllable materials variable.[239] Energy-relevant templating also benefits from multi-compartment carriers. A Lego-style glass capillary device forms O/O/W and W/O/W double emulsions to microencapsulate both organic and hydrated-salt phase change materials while enabling shell compositing.[80]

Beyond oil-based systems, all-aqueous complex emulsions based on aqueous two-phase systems (ATPS) serve as soft templates for porous hydrogel microparticles. Using such droplets as placeholders, porous GelMA microspheres with tunable pore architecture support spatially controlled three-dimensional co-culture, for example HUVECs in pores and HepG2 in the matrix, which broadens tissue model design beyond single-core carriers.[240]

For materials-oriented implementations, complex emulsions also provide a versatile platform for templating solid microstructures with optical or thermal functionality derived from interfacial organization. Kim *et al.* used microfluidic double emulsions to template robust core–shell microcapsules containing chiral mesogens that self-assemble into cholesteric order, yielding thermochromic structural color (Fig. 9G).[241] The optical response shifts continuously with temperature while the shell preserves integrity during handling, which makes the capsules practical as readable, reconfigurable labels and local temperature reporters. This illustrates how complex emulsion templating translates interfacial alignment into functional photonic outputs in an application-ready form.

Translating these capabilities beyond bespoke single-channel demonstrations depends on platform-level solutions for wettability fidelity and device tuning. Wu *et al.* lithographically patterned wettability on all channel surfaces in silicon–glass devices, maintained silane stability through processes such as anodic bonding, and enabled parallelized double emulsion generation with consistent behavior across arrays, directly addressing throughput and reproducibility requirements.[73] In parallel, Lashkaripour *et al.* compiled a broad droplet dataset and trained machine learning models that predict device geometries and operating conditions for stable single and double emulsions from roughly 15 to 250 μm and up to approximately 12 kHz, which reduces trial-and-error when porting applications across fluids, sizes, and materials.[242] Alongside the application-focused synthesis by Kim *et al.*, which highlights how microfluidic emulsification and parallelization transform metastable droplets into functional microcapsules with programmed shells, these advances outline a practical design logic in which wettability control stabilizes the generation window and core–shell compositions are specified to regulate transport and release.[243] Together with the assay and materials examples above,[80,229,232,235,240] these capabilities integrate on-demand reagent addition, incubation, sorting, and solidification within a single platform, enabling staged chemistries, high-throughput bioassays, hierarchically structured materials, and application modules spanning energy, photonics, and soft-matter or biological delivery.

6. Conclusion and outlook

3D printing converts digital designs directly into sealed, volumetric microfluidic devices, which makes it particularly well suited to droplet generation. In a single build, it can realize vertical step emulsifiers, curved three-dimensional junctions, and embedded distribution manifolds as a monolith, thereby reducing operator dependence and accelerating design iteration. When geometry, printable resin, and post-cure surface conditioning are co-designed, the channel wall affinity to the working phase becomes stable and the usable dripping window broadens. This co-optimization enables reproducible production of monodisperse emulsions and well-matched outputs across nozzle arrays from pilot prototypes to wafer-scale runs.

Beyond layer-wise SLA and DLP, emerging photopolymer platforms provide microfluidics-specific advantages for chip-scale production. Continuous printing, exemplified by continuous liquid interface production[180] and high-area rapid printing,[244] yields long, smooth channel segments and high part counts in a single run. In droplet devices, this supports dense parallel nozzle arrays with improved wall finish, near-axial isotropy, and more uniform manifold delivery, which broadens stable dripping regimes and narrows size distributions. Volumetric approaches, typified by computed axial lithography, create support-free enclosed networks with short vertical interconnects and out-of-plane routing.[245] This capability allows distribution manifolds, vertical step emulsifiers, and coaxial or nested junctions to be fabricated in one piece with minimal dead volume. As these platforms see wider adoption in microfluidic manufacturing, they are likely to extend practical resolution, reduce channel roughness and height-dependent dimensional drift, and enable spatially programmed materials or surface states to be embedded within sealed channels. Taken together, these advances shift the field from rapid prototyping toward predictable and scalable production of robust generators for both single and complex emulsions.

Recent advances in wavelength-selective, one-vat vat-photopolymerization provide a single-bath route to multimaterial printing without resin exchange or intermediate washing. In a hybrid epoxy–acrylate formulation, Kim *et al.* designed two orthogonal photopolymerization pathways that can be activated independently by different wavelengths.[246] Short-wavelength exposure drives cationic curing of the epoxy and yields stiff, glass-like domains, while long-wavelength exposure initiates radical polymerization of the acrylate and forms soft, elastomeric regions. Within one continuous build, hard and soft segments are positioned at the voxel level and are covalently integrated across their interfaces, producing monolithic parts that exhibit large mechanical contrast while maintaining interfacial continuity and dimensional fidelity. Building on the same concept, Mason *et al.* co-printed dissolvable sacrificial supports in the same vat and removed them after printing.[247] This post-print dissolution step released suspended and overhanging features that were previously inaccessible with conventional vat-photopolymerization, while both the functional structure and its temporary support were formed simultaneously during fabrication.

Looking ahead, this single-vat, dual-wavelength framework offers a promising route to embed surface-energy contrast directly within sealed channels for droplet microfluidics. A single resin could be molecularly designed so that each curing pathway produces a network with different wettability, one relatively hydrophilic and the other hydrophobic. By locally varying the exposure wavelength during printing, regions of the same monolithic device can be rendered hydrophilic or hydrophobic. This spatial programming of surface energy allows O/W and W/O emulsion operation to be selectively controlled within a single design. Such *in situ* surface programming removes the need for plasma activation, silanization, or coating-based post-processing, which can age or compromise optical clarity. Extending this approach to multiple wetting regions could enable fully printed generators capable of producing double and higher-order emulsions without external surface modification. While this remains forward-looking, the optical orthogonality, interfacial integrity, and simultaneous structure-plus-support printing already demonstrated provide a solid foundation for the next generation of as-printed droplet systems.

Ongoing progress in printing resolution, materials, and *in situ* surface programming has substantially reduced fabrication-induced variability at the device level and expanded the accessible operating space for droplet generators. However, as 3D-printed droplet microfluidic systems progress toward dense parallelization, long-term operation, and production-relevant throughput, residual variations in geometry, surface state, and flow distribution remain difficult to eliminate through fabrication control alone. These system- and operation-level uncertainties motivate complementary strategies that integrate additive manufacturing with data-driven modeling and feedback.

While 3D printing technologies have advanced rapidly, several challenges remain before droplet microfluidic devices can transition from prototyping tools to reliable manufacturing platforms. Key issues include long-term wettability stability under continuous operation, resin-fluid chemical compatibility, and aging- or leaching-induced performance degradation. In particular, optical scattering, overcuring, and post-curing deformation constrain the minimum achievable feature size and channel fidelity, particularly in enclosed microfluidic geometries, which can adversely affect flow uniformity and droplet formation, thereby hindering the reliable translation of 3D-printed droplet microfluidics beyond laboratory-scale demonstrations.

Although interest in data-driven design and digital twins for droplet microfluidics is growing, their direct translation to 3D-printed devices remains fundamentally constrained by fabrication-induced non-idealities. In additively

manufactured microfluidic systems, the designed CAD geometry is often not reproduced exactly in the as-printed device due to resolution limits, tolerance stack-up, and post-processing variability. Deviations in critical dimensions, such as effective throat width or step height, together with surface roughness, incomplete feature definition, and time-dependent surface-state evolution, can shift droplet formation regimes and narrow operational stability windows. These effects are particularly pronounced in droplet generators, where small geometric or wetting perturbations may trigger regime transitions, wetting failure, or loss of monodispersity during extended operation.

As a result, predictive models that assume idealized geometry and static surface properties often fail to capture the device-to-device variability and performance drift observed in 3D-printed systems. This mismatch between design intent and the as-printed device state motivates the development of print-aware digital twin frameworks, in which fabrication-induced deviations and evolving surface conditions are explicitly incorporated into the model description rather than treated as secondary uncertainties.

In this context, recent AI-enabled studies in droplet microfluidics provide important methodological building blocks, while also highlighting the gap that must be addressed for 3D-printed devices. Hormozinezhad *et al.* have demonstrated that combining dimensional analysis with neural networks can efficiently identify flow conditions yielding targeted droplet outcomes.[248] Also, Shin *et al.* reported that AI-guided flow control enables rapid exploration of broad parametric spaces for double-emulsion generation (Fig. 10A).[249] From a design perspective, open environments such as Flui3d integrate geometry generation, simulation, and optimization, lowering the barrier for translating learned models into printable device layouts (Fig. 10B).[250] However, these approaches typically assume idealized geometry and static surface properties, or rely on empirically tuned representations of the physical device. As a result, their direct applicability to 3D-printed droplet generators remains limited, since fabrication-induced deviations in critical dimensions, surface roughness, and wettability are not explicitly incorporated within the learning loop. Thus, these studies highlight the need to advance AI-assisted workflows toward print-aware frameworks that explicitly account for the as-printed device state, representing a necessary step toward robust digital twins for additively manufactured droplet microfluidic systems.

From a translational perspective, these considerations closely align with the requirements for industrial deployment of 3D-printed droplet microfluidic systems. Although additive manufacturing enables rapid prototyping and complex three-dimensional architectures, variability in feature resolution, surface finish, and resin aging remains a major barrier to long-term reproducibility and regulatory acceptance. Addressing these challenges requires standardized design rules, validated printing and post-curing protocols, and metrology strategies that directly link critical dimensions and surface state to droplet performance.

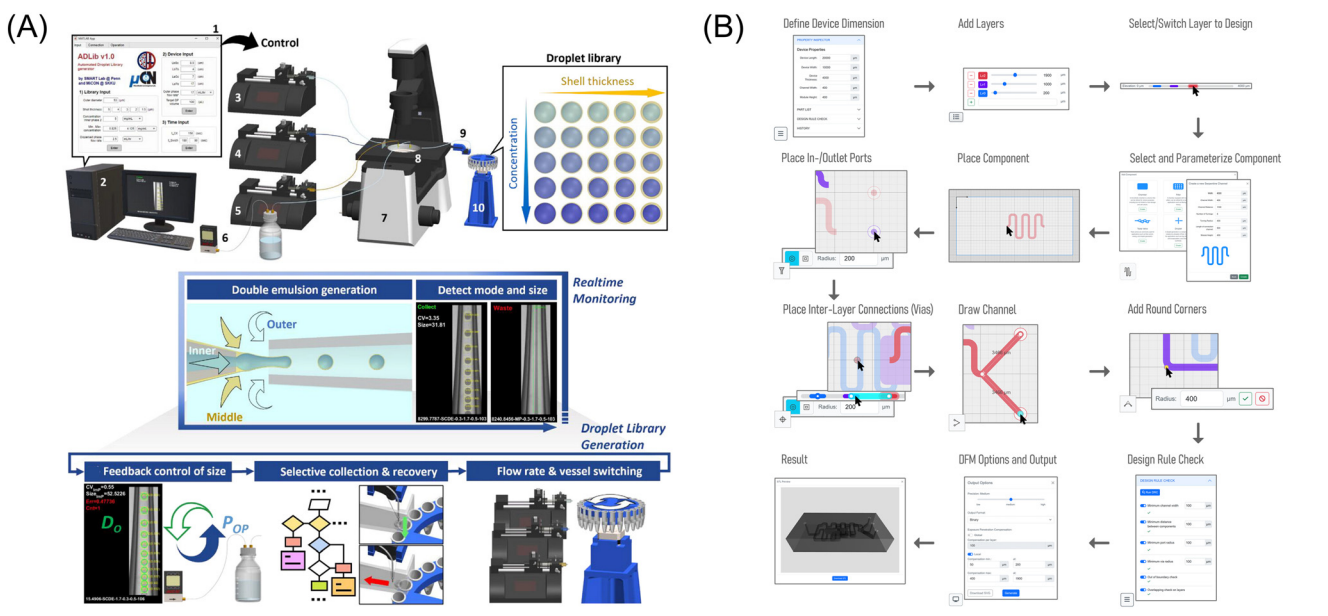

Fig. 10 Integration of AI and digital twins for predictive design and automated operation of droplet microfluidic devices. A) AI-assisted automated double emulsion library generation platform, capable of real-time monitoring, adaptive control of droplet size, and autonomous adjustment of flow parameters. This figure has been reproduced from ref. 249 under the Creative Commons Attribution License (CC BY 4.0). B) Workflow of the open-source digital design platform Flui3d, illustrating stepwise virtual prototyping of 3D-printed microfluidic devices from component selection and interlayer connections to geometry validation and final device export. This figure has been reproduced from ref. 250 under the Creative Commons Attribution License (CC BY 4.0).

In this context, reference artifacts and calibration coupons targeting the smallest vias, narrowest throats, and most wetting-sensitive regions should be incorporated into routine quality control, together with statistically defined acceptance windows for CAH, surface roughness, and optical transmission. Within such a framework, print-aware digital twins can facilitate automated post-fabrication calibration and qualification, thereby reducing device-to-device variability and stabilizing operation in parallelized architectures. As these practices mature, 3D-printed droplet generators are expected to evolve from devices adjusted once at setup into platforms capable of maintaining consistent performance across extended production runs and complex emulsion workflows.

Building on these considerations, a practical AI-digital twin framework for 3D-printed droplet microfluidics should be formulated as a calibration- and uncertainty-aware closed-loop, rather than as a purely predictive engine. In this architecture, surrogate models are first trained using a combination of simulations and targeted experiments to capture sensitivities to capillary number, viscosity ratio, and nominal geometric descriptors. These models are then updated using post-fabrication metrology that quantifies as-printed critical dimensions, surface roughness, and wettability metrics, thereby estimating the effective device state relevant to droplet formation.

During operation, sensor feedback such as optical droplet sizing or pressure measurements enables detection of performance drift arising from surface aging, surfactant depletion, or thermal fluctuations. Iterative model updating and recalibration allow operating windows to be adjusted in response to fabrication tolerances and time-dependent changes, rather than assuming static, ideal behavior. Within this framework, AI methods such as Bayesian optimization or active learning primarily function to manage uncertainty and reduce experimental burden, while full digital twins are most valuable during design and qualification. Framed in this way, AI-assisted digital twins enable robust operation by reconciling design intent with the evolving physical state of 3D-printed droplet generators.

Material certification is also a parallel priority. Applications in biomedicine, food, and pharmaceuticals demand resins with demonstrated biocompatibility, solvent resistance, and low extractables under sterilization and use conditions. While multi-material printing now enables hydrophilic to hydrophobic patterning and embedded sensing, only a small subset of printable chemistries currently aligns with stringent standards for cytotoxicity, sensitization, and chemical compatibility. Coordinated efforts among materials scientists, regulatory experts, and device engineers are needed to expand the portfolio of certified resins, to define acceptable post-processing workflows, and to establish documentation packages that support submissions under relevant quality systems.

Scalability is also a concern. Arrays with tens to hundreds of generators have been demonstrated, yet production at liter-per-day scales requires closed-loop assurance of uniform flow distribution and droplet monodispersity. A practical path forward couples CFD and AI-based design automation with standardized additive workflows and in-line sensing. Hydraulic network models and surrogate predictors can set geometry and operating points that are resilient to tolerance stack-up. Embedded pressure taps, optical drop sizing, and flow meters provide data for real-time feedback control and for batch release criteria. Together with process qualification and ongoing statistical process control, these steps can close the gap between laboratory prototypes and regulated, high-throughput manufacturing.

The continued convergence of 3D printing and AI points toward fully integrated, programmable, and adaptive droplet microfluidic systems. The approach is to move beyond passive channel networks and to fabricate complete functional platforms in a single monolithic step that includes embedded sensors, actuators, and standardized interfaces for control and data. In such a workflow, a user specifies target properties such as droplet size, shell thickness, composition, and throughput in a simple interface. An AI engine, linked to a digital twin of the device and process, then performs inverse design to select geometry, materials, and operating conditions, followed by immediate on-site fabrication on a compatible printer. During operation, integrated pressure, flow, and optical sensors stream data to lightweight models that estimate states such as capillary number, wettability drift, and maldistribution. A closed-loop controller adjusts flow rates, temperature, or manifold selection in real-time to maintain monodispersity and yield under perturbations that include surfactant depletion, temperature variation, or gradual changes in surface energy. Realizing this vision will require a shared stack that links CAD, slicers, materials library, simulation, and control, together with validated print and post-cure recipes and interoperable data formats. It will also require certified resins and coatings with documented biocompatibility, solvent resistance, and aging profiles so that digital prescriptions map to compliant hardware. As these elements mature, droplet generators will shift from devices that are tuned once and left to drift, to self-calibrating production platforms that learn and retune their own operating envelopes while delivering customized single and complex emulsions at industrially relevant scales.

Author contributions

Je Hyun Lee: investigation (literature search); writing – original draft; writing – review & editing. Taesoo Jang: investigation (literature search); writing – original draft; writing – review & editing. Soeun Park: investigation (literature search); writing – original draft. Su-Bin Shin: investigation (literature search); writing – original draft. Jaemoon Lee: investigation (literature search); writing – original draft. Yoon-Ho Hwang: conceptualization;

supervision; writing – review & editing. Hyomin Lee: conceptualization; supervision; writing – review & editing.

Conflicts of interest

There are no conflicts to declare.

Data availability

No primary research results, software or code have been included and no new data were generated or analysed as part of this review.

Acknowledgements

This work was supported by a grant of the Korea Health Technology R&D Project through the Korea Health Industry Development Institute (KHIDI), funded by the Ministry of Health & Welfare, Republic of Korea (No. RS-2025-02214418).

References

1 P. Neužil, S. Giselbrecht, K. Länge, T. J. Huang and A. Manz, *Nat. Rev. Drug Discovery*, 2012, **11**, 620–632.
2 C.-X. Zhao, *Adv. Drug Delivery Rev.*, 2013, **65**, 1420–1446.
3 L. Zhang, Y. Hu and L. Jiang, *Compr. Rev. Food Sci. Food Saf.*, 2024, **23**, e70043.
4 D. Venkataramani, A. Tsulaia and S. Amin, *Adv. Colloid Interface Sci.*, 2020, **283**, 102234.
5 W. Li, L. Zhang, X. Ge, B. Xu, W. Zhang, L. Qu, C.-H. Choi, J. Xu, A. Zhang, H. Lee and D. A. Weitz, *Chem. Soc. Rev.*, 2018, **47**, 5646–5683.
6 Y. Zeng, J. W. Khor, T. L. van Neel, W.-C. Tu, J. Berthier, S. Thongpang, E. Berthier and A. B. Theberge, *Nat. Rev. Chem.*, 2023, **7**, 439–455.
7 J. Wu, S. Yadavali, D. Lee and D. A. Issadore, *Appl. Phys. Rev.*, 2021, **8**, 031304.
8 T. Moragues, D. Arguijo, T. Beneyton, C. Modavi, K. Simutis, A. R. Abate, J.-C. Baret, A. J. deMello, D. Densmore and A. D. Griffiths, *Nat. Rev. Methods Primers*, 2023, **3**, 32.
9 H. Seo and H. Lee, *Biomicrofluidics*, 2021, **15**, 021301.
10 Y. Oh and S.-H. Kim, *Langmuir*, 2024, **40**, 19166–19175.
11 J. H. Lee, C.-H. Choi and H. Lee, *Adv. Funct. Mater.*, 2025, **35**, 2417921.
12 P. Zhu and L. Wang, *Lab Chip*, 2017, **17**, 34–75.
13 K. S. Elvira, F. Gielen, S. S. H. Tsai and A. M. Nightingale, *Lab Chip*, 2022, **22**, 859–875.
14 A. J. Capel, R. P. Rimington, M. P. Lewis and S. D. R. Christie, *Nat. Rev. Chem.*, 2018, **2**, 422–436.
15 T. J. Wallin, J. Pikul and R. F. Shepherd, *Nat. Rev. Mater.*, 2018, **3**, 84–100.
16 S. O'Halloran, A. Pandit, A. Heise and A. Kellett, *Adv. Sci.*, 2023, **10**, 2204072.
17 N. Bhattacharjee, A. Urrios, S. Kang and A. Folch, *Lab Chip*, 2016, **16**, 1720–1742.
18 L. A. Milton, M. S. Viglione, L. J. Y. Ong, G. P. Nordin and Y.-C. Toh, *Lab Chip*, 2023, **23**, 3537–3560.
19 Q. Ji, J. M. Zhang, Y. Liu, X. Li, P. Lv, D. Jin and H. Duan, *Sci. Rep.*, 2018, **8**, 4791.
20 A. V. Nielsen, M. J. Beauchamp, G. P. Nordin and A. T. Woolley, *Annu. Rev. Anal. Chem.*, 2020, **13**, 45–65.
21 N. Zhang, Z. Wang, Z. Zhao, D. Zhang, J. Feng, L. Yu, Z. Lin, Q. Guo, J. Huang, J. Mao and J. Yang, *Microsyst. Nanoeng.*, 2025, **11**, 35.
22 N. Gyimah, O. Scheler, T. Rang and T. Pardy, *Micromachines*, 2021, **12**, 339.
23 C. A. Warr, N. G. Crawford, G. P. Nordin and W. G. Pitt, *Micromachines*, 2023, **14**, 6.
24 T. M. Squires and S. R. Quake, *Rev. Mod. Phys.*, 2005, **77**, 977–1026.
25 H. A. Stone, A. D. Stroock and A. Ajdari, *Annu. Rev. Fluid Mech.*, 2004, **36**, 381–411.
26 R. Seemann, M. Brinkmann, T. Pfohl and S. Herminghaus, *Rep. Prog. Phys.*, 2012, **75**, 016601.
27 C. N. Baroud, F. Gallaire and R. Dangla, *Lab Chip*, 2010, **10**, 2032–2045.
28 J. K. Nunes, S. S. H. Tsai, J. Wan and H. A. Stone, *J. Phys. D: Appl. Phys.*, 2013, **46**, 114002.
29 S. L. Anna, *Annu. Rev. Fluid Mech.*, 2016, **48**, 285–309.
30 M. P. Boruah, P. R. Randive and S. Pati, *Phys. Fluids*, 2024, **36**, 121301.
31 Z. Z. Chong, S. H. Tan, A. M. Gañán-Calvo, S. B. Tor, N. H. Loh and N.-T. Nguyen, *Lab Chip*, 2016, **16**, 35–58.
32 M. Ali, W. Kim, M. S. Khan, M. A. Sahin, G. Destgeer and J. Park, *Biomicrofluidics*, 2025, **19**, 031502.
33 G.-P. Zhu, Q.-Y. Wang, Z.-K. Ma, S.-H. Wu and Y.-P. Guo, *Biosensors*, 2022, **12**, 156.
34 T. Fu, Y. Wu, Y. Ma and H. Z. Li, *Chem. Eng. Sci.*, 2012, **84**, 207–217.
35 M. De Menech, P. Garstecki, F. Jousse and H. A. Stone, *J. Fluid Mech.*, 2008, **595**, 141–161.
36 L. Cai, J. Marthelot and P. T. Brun, *Proc. Natl. Acad. Sci. U. S. A.*, 2019, **116**, 22966–22971.
37 A. S. Utada, A. Fernandez-Nieves, H. A. Stone and D. A. Weitz, *Phys. Rev. Lett.*, 2007, **99**, 094502.
38 S. G. Sontti and A. Atta, *Phys. Fluids*, 2023, **35**, 012010.
39 M. L. Eggersdorfer, H. Seybold, A. Ofner, D. A. Weitz and A. R. Studart, *Proc. Natl. Acad. Sci. U. S. A.*, 2018, **115**, 9479–9484.
40 P. Garstecki, M. J. Fuerstman, H. A. Stone and G. M. Whitesides, *Lab Chip*, 2006, **6**, 437–446.
41 S. L. Anna, N. Bontoux and H. A. Stone, *Appl. Phys. Lett.*, 2003, **82**, 364–366.
42 W.-C. Jeong, J.-M. Lim, J.-H. Choi, J.-H. Kim, Y.-J. Lee, S.-H. Kim, G. Lee, J.-D. Kim, G.-R. Yi and S.-M. Yang, *Lab Chip*, 2012, **12**, 1446–1453.
43 Y. Chen, L. Wu and C. Zhang, *Phys. Rev. E*, 2013, **87**, 013002.
44 S. Barkley, S. J. Scarfe, E. R. Weeks and K. Dalnoki-Veress, *Soft Matter*, 2016, **12**, 7398–7404.
45 T. Deydier, G. Bolognesi and G. T. Vladisavljević, *Colloids Surf., A*, 2022, **641**, 128439.
46 H. B. Eral, D. J. C. M. 't Mannetje and J. M. Oh, *Colloid Polym. Sci.*, 2013, **291**, 247–260.

47 W. Li, Z. Nie, H. Zhang, C. Paquet, M. Seo, P. Garstecki and E. Kumacheva, *Langmuir*, 2007, **23**, 8010–8014.
48 S. C. Kim, D. J. Sukovich and A. R. Abate, *Lab Chip*, 2015, **15**, 3163–3169.
49 C.-H. Choi, H. Lee and D. A. Weitz, *ACS Appl. Mater. Interfaces*, 2018, **10**, 3170–3174.
50 J. L. Fritz and M. J. Owen, *J. Adhes.*, 1995, **54**, 33–45.
51 S. H. Tan, N.-T. Nguyen, Y. C. Chua and T. G. Kang, *Biomicrofluidics*, 2010, **4**, 032204.
52 T. Trantidou, Y. Elani, E. Parsons and O. Ces, *Microsyst. Nanoeng.*, 2017, **3**, 16091.
53 A. Fatona, Y. Chen, M. Reid, M. A. Brook and J. M. Moran-Mirabal, *Lab Chip*, 2015, **15**, 4322–4330.
54 A. Oláh, H. Hillborg and G. J. Vancso, *Appl. Surf. Sci.*, 2005, **239**, 410–423.
55 V. Silverio, P. A. G. Canane and S. Cardoso, *Colloids Surf., A*, 2019, **570**, 210–217.
56 T. Yang, J. Choo, S. Stavrakis and A. de Mello, *Chem. – Eur. J.*, 2018, **24**, 12078–12083.
57 N. Li and C.-M. Ho, *Lab Chip*, 2008, **8**, 2105–2112.
58 E. Ul-Haq, S. Patole, M. Moxey, E. Amstad, C. Vasilev, C. N. Hunter, G. J. Leggett, N. D. Spencer and N. H. Williams, *ACS Nano*, 2013, **7**, 7610–7618.
59 P. Jiang, S.-Y. Li, H. Sugimura and O. Takai, *Appl. Surf. Sci.*, 2006, **252**, 4230–4235.
60 Y. Chen, E. T. Kang, K. G. Neoh and W. Huang, *Langmuir*, 2001, **17**, 7425–7432.
61 S. Mahapatra, D. Bodas, A. B. Mandale, S. A. Gangal and V. N. Bhoraskar, *Mater. Lett.*, 2006, **60**, 1360–1365.
62 H. Li, K. Sheng, Z. Chen, S. Hao, Z. Zhou, Z. Zhang, X. Liu, M. Xiong, Y. Gu and J. Huang, *Ind. Chem. Mater.*, 2024, **2**, 458–468.
63 M. Li, B. Su, B. Zhou, H. Wang and J. Meng, *Appl. Surf. Sci.*, 2020, **508**, 145187.
64 D. Kosoff, J. Yu, V. Suresh, D. J. Beebe and J. M. Lang, *Lab Chip*, 2018, **18**, 3011–3017.
65 M. Jang, C. K. Park and N. Y. Lee, *Sens. Actuators, B*, 2014, **193**, 599–607.
66 T. Rohr, D. F. Ogletree, F. Svec and J. M. J. Fréchet, *Adv. Funct. Mater.*, 2003, **13**, 264–270.
67 Y. Lee, J. K. Kim, S. Chung, C. Chung, J. K. Chang and J. Y. Yoo, *Proc. 2nd Annu. Int. IEEE-EMBS Special Topic Conf. Microtechnologies in Medicine and Biology*, 2002, pp. 560–564.
68 T. W. Bacha, D. C. Manuguerra, R. A. Marano and J. F. Stanzione, *RSC Adv.*, 2021, **11**, 21745–21753.
69 M. A. Catterton, A. N. Montalbine and R. R. Pompano, *Langmuir*, 2021, **37**, 7341–7348.
70 C.-N. Hsu, N. P. Mai, H.-K. Chang and P.-Y. Chen, *Polymers*, 2024, **16**, 1874.
71 V.-T. Nguyen, E. Park, N.-A. Nguyen, O. Omelianovych, L. L. Larina, S. Sajid Hussain and H.-S. Choi, *Appl. Surf. Sci.*, 2023, **615**, 156418.
72 A. Makhinia, P. Azizian, V. Beni, J. Casals-Terré, J. M. Cabot and P. Andersson Ersman, *Adv. Mater. Technol.*, 2023, **8**, 2300127.
73 J. Wu, Y.-H. Hwang, S. Yadavali, D. Lee and D. A. Issadore, *Adv. Funct. Mater.*, 2024, **34**, 2309718.
74 M. Azarmanesh, M. Farhadi and P. Azizian, *Phys. Fluids*, 2016, **28**, 032005.
75 H. Hillborg, M. Sandelin and U. W. Gedde, *Polymer*, 2001, **42**, 7349–7362.
76 J. N. Lee, C. Park and G. M. Whitesides, *Anal. Chem.*, 2003, **75**, 6544–6554.
77 Y. Mao, I. Pechenizkiy, T. Stieglitz and T. Doll, *Micromachines*, 2021, 12.
78 C. Chircov and A. M. Grumezescu, *Micromachines*, 2022, **13**, 164.
79 Y. Wei, T. Wang, Y. Wang, S. Zeng, Y.-P. Ho and H.-P. Ho, *Micromachines*, 2023, **14**, 656.
80 S. Parvate, G. T. Vladisavljević, N. Leister, A. Spyrou, G. Bolognesi, D. Baiocco, Z. Zhang and S. Chattopadhyay, *ACS Appl. Mater. Interfaces*, 2023, **15**, 17195–17210.
81 Y. W. Adugna, A. D. Akessa and H. G. Lemu, *IOP Conf. Ser.: Mater. Sci. Eng.*, 2021, **1201**, 012041.
82 3D systems homepage, https://www.3dsystems.com/.
83 3Dresyns homepage, https://www.3dresyns.com/.
84 Boston Microfabrication homepage, https://bmf3d.com/.
85 EnvisionTec homepage, https://etec.desktopmetal.com/.
86 Formlabs homepage, https://formlabs.com/.
87 MiiCraft homepage, https://miicraft.com/.
88 Stratasys homepage, https://www.stratasys.com/en/.
89 C. M. B. Ho, S. H. Ng, K. H. H. Li and Y.-J. Yoon, *Lab Chip*, 2015, **15**, 3627–3637.
90 X. Fu, B. Zou, H. Xing, L. Li, Y. Li and X. Wang, *Ceram. Int.*, 2019, **45**, 17630–17637.
91 A. Bove, F. Calignano, M. Galati and L. Iuliano, *Appl. Sci.*, 2022, **12**, 3591.
92 Z. Weng, X. Huang, S. Peng, L. Zheng and L. Wu, *Nat. Commun.*, 2023, **14**, 4303.
93 W. Li, M. Wang, H. Ma, F. A. Chapa-Villarreal, A. O. Lobo and Y. S. Zhang, *iScience*, 2023, **26**, 106039.
94 S. C. Ligon, R. Liska, J. Stampfl, M. Gurr and R. Mülhaupt, *Chem. Rev.*, 2017, **117**, 10212–10290.
95 G. Gonzalez, I. Roppolo, C. F. Pirri and A. Chiappone, *Addit. Manuf.*, 2022, **55**, 102867.
96 A. Naderi, N. Bhattacharjee and A. Folch, *Annu. Rev. Biomed. Eng.*, 2019, **21**, 325–364.
97 S. Waheed, J. M. Cabot, N. P. Macdonald, T. Lewis, R. M. Guijt, B. Paull and M. C. Breadmore, *Lab Chip*, 2016, **16**, 1993–2013.
98 Ö. M. Yüceer, E. Kaynak Öztürk, E. S. Çiçek, N. Aktaş and M. Bankoğlu Güngör, *Polymers*, 2025, **17**, 316.
99 H. Gong, B. P. Bickham, A. T. Woolley and G. P. Nordin, *Lab Chip*, 2017, **17**, 2899–2909.
100 A. K. Au, N. Bhattacharjee, L. F. Horowitz, T. C. Chang and A. Folch, *Lab Chip*, 2015, **15**, 1934–1941.
101 R. Chaudhary, P. Fabbri, E. Leoni, F. Mazzanti, R. Akbari and C. Antonini, *Prog. Addit. Manuf.*, 2023, **8**, 331–351.
102 X. Wang, J. Liu, Y. Zhang, P. M. Kristiansen, A. Islam, M. Gilchrist and N. Zhang, *Virtual Phys. Prototyp.*, 2023, **18**, e2248101.
103 H. Wang, B. Zhang, J. Zhang, X. He, F. Liu, J. Cui, Z. Lu, G. Hu, J. Yang, Z. Zhou, R. Wang, X. Hou, L. Ma, P. Ren, Q.

Ge, P. Li and W. Huang, *ACS Appl. Mater. Interfaces*, 2021, **13**, 55507–55516.
104 P. J. E. M. van der Linden, A. M. Popov and D. Pontoni, *Lab Chip*, 2020, **20**, 4128–4140.
105 J. Chen, S. Huang, Y. Long, K. Wang, Y. Guan, L. Hou, B. Dai, S. Zhuang and D. Zhang, *Biosensors*, 2022, **12**, 1085.
106 Z. Luo, H. Zhang, R. Chen, H. Li, F. Cheng, L. Zhang, J. Liu, T. Kong, Y. Zhang and H. Wang, *Microsyst. Nanoeng.*, 2023, **9**, 103.
107 J.-W. Kang, J. Jeon, J.-Y. Lee, J.-H. Jeon and J. Hong, *Micromachines*, 2024, **15**, 61.
108 C. N. LaFratta and T. Baldacchini, *Micromachines*, 2017, **8**, 101.
109 Z. Faraji Rad, P. D. Prewett and G. J. Davies, *Microsyst. Nanoeng.*, 2021, **7**, 71.
110 A. I. Ciuciu and P. J. Cywiński, *RSC Adv.*, 2014, **4**, 45504–45516.
111 X. Jing, H. Fu, B. Yu, M. Sun and L. Wang, *Front. Bioeng. Biotechnol.*, 2022, **10**, 2022.
112 S. D. Gittard, A. Ovsianikov, B. N. Chichkov, A. Doraiswamy and R. J. Narayan, *Expert Opin. Drug Deliv.*, 2010, **7**, 513–533.
113 Y. Liu, D. D. Nolte and L. J. Pyrak-Nolte, *Appl. Phys. A: Mater. Sci. Process.*, 2010, **100**, 181–191.
114 A. Selimis, V. Mironov and M. Farsari, *Microelectron. Eng.*, 2015, **132**, 83–89.
115 M. A. Brown, K. M. Zappitelli, L. Singh, R. C. Yuan, M. Bemrose, V. Brogden, D. J. Miller, M. C. Smear, S. F. Cogan and T. J. Gardner, *Nat. Commun.*, 2023, **14**, 3610.
116 O. M. Young, X. Xu, S. Sarker and R. D. Sochol, *Lab Chip*, 2024, **24**, 2371–2396.
117 G. M. Fortunato, M. Nicoletta, E. Batoni, G. Vozzi and C. De Maria, *Addit. Manuf.*, 2023, **69**, 103541.
118 S. Salifu, D. Desai, O. Ogunbiyi and K. Mwale, *Int. J. Adv. Manuf. Technol.*, 2022, **119**, 6877–6891.
119 A. Cano-Vicent, M. M. Tambuwala, S. S. Hassan, D. Barh, A. A. A. Aljabali, M. Birkett, A. Arjunan and Á. Serrano-Aroca, *Addit. Manuf.*, 2021, **47**, 102378.
120 G. Berglund, A. Wisniowiecki, J. Gawedzinski, B. Applegate and T. S. Tkaczyk, *Optica*, 2022, **9**, 623–638.
121 V. Romanov, R. Samuel, M. Chaharlang, A. R. Jafek, A. Frost and B. K. Gale, *Anal. Chem.*, 2018, **90**, 10450–10456.
122 A. B. Zia, J. Farrell and I. G. Foulds, *Lab Chip*, 2024, **24**, 3015–3026.
123 O. Gülcan, K. Günaydın and A. Tamer, *Polymers*, 2021, **13**, 2829.
124 L.-Y. Zhou, J. Fu and Y. He, *Adv. Funct. Mater.*, 2020, **30**, 2000187.
125 A. Bagheri and J. Jin, *ACS Appl. Polym. Mater.*, 2019, **1**, 593–611.
126 P. Patpatiya, K. Chaudhary, A. Shastri and S. Sharma, *Proc. Inst. Mech. Eng. Part C J. Mech. Eng. Sci.*, 2022, **236**, 7899–7926.
127 J. Xu, M. Harasek and M. Gföhler, *Polymers*, 2025, **17**, 455.
128 G. K. Monia Kabandana, T. Zhang and C. Chen, *Anal. Methods*, 2022, **14**, 2885–2906.
129 H. B. Musgrove, S. R. Cook and R. R. Pompano, *ACS Appl. Bio Mater.*, 2023, **6**, 3079–3083.
130 B. J. O'Grady, M. D. Geuy, H. Kim, K. M. Balotin, E. R. Allchin, D. C. Florian, N. N. Bute, T. E. Scott, G. B. Lowen, C. M. Fricker, M. L. Fitzgerald, S. A. Guelcher, J. P. Wikswo, L. M. Bellan and E. S. Lippmann, *Lab Chip*, 2021, **21**, 4814–4822.
131 C. A. Warr, H. S. Hinnen, S. Avery, R. J. Cate, G. P. Nordin and W. G. Pitt, *Micromachines*, 2021, **12**, 91.
132 M. Ziaee and N. B. Crane, *Addit. Manuf.*, 2019, **28**, 781–801.
133 K. Zhao, Z. Su, Z. Ye, W. Cao, J. Pang, X. Wang, Z. Wang, X. Xu and J. Zhu, *J. Mater. Res. Technol.*, 2023, **27**, 5449–5469.
134 C. A. Chatham, T. E. Long and C. B. Williams, *Prog. Polym. Sci.*, 2019, **93**, 68–95.
135 F. E. Jabri, A. Ouballouch, L. Lasri and R. El Alaiji, *J. Achiev. Mater. Manuf. Eng.*, 2023, **118**, 5–17.
136 A. P. Golhin, R. Tonello, J. R. Frisvad, S. Grammatikos and A. Strandlie, *Int. J. Adv. Manuf. Technol.*, 2023, **127**, 987–1043.
137 M. U. Azam, I. Belyamani, A. Schiffer, S. Kumar and K. Askar, *J. Mater. Res. Technol.*, 2024, **30**, 9625–9646.
138 J. M. Zhang, Q. Ji and H. Duan, *Micromachines*, 2019, **10**, 754.
139 L. H. Duong and P.-C. Chen, *Biomicrofluidics*, 2019, **13**, 024108.
140 Y. Alapan, M. N. Hasan, R. Shen and U. A. Gurkan, *J. Nanotechnol. Eng. Med.*, 2015, **6**, 021007.
141 X. Peng, X. Kuang, D. J. Roach, Y. Wang, C. M. Hamel, C. Lu and H. J. Qi, *Addit. Manuf.*, 2021, **40**, 101911.
142 Y. T. Kim, A. Ahmadianyazdi and A. Folch, *Nat. Protoc.*, 2023, **18**, 1243–1259.
143 A. Sharaf, J. P. Frimat, G. J. Kremers and A. Accardo, *Micro Nano Eng.*, 2023, **19**, 100188.
144 R. Su, F. Wang and M. C. McAlpine, *Lab Chip*, 2023, **23**, 1279–1299.
145 A. K. Au, W. Huynh, L. F. Horowitz and A. Folch, *Angew. Chem., Int. Ed.*, 2016, **55**, 3862–3881.
146 C. Yu, J. Schimelman, P. Wang, K. L. Miller, X. Ma, S. You, J. Guan, B. Sun, W. Zhu and S. Chen, *Chem. Rev.*, 2020, **120**, 10695–10743.
147 D. Böcherer, Y. Li, C. Rein, S. Franco Corredor, P. Hou and D. Helmer, *Adv. Funct. Mater.*, 2024, **34**, 2401516.
148 G. Lu, R. Tang, J. Nie and X. Zhu, *Macromol. Rapid Commun.*, 2024, **45**, 2300661.
149 K. S. Lim, R. Levato, P. F. Costa, M. D. Castilho, C. R. Alcala-Orozco, K. M. A. van Dorenmalen, F. P. W. Melchels, D. Gawlitta, G. J. Hooper, J. Malda and T. B. F. Woodfield, *Biofabrication*, 2018, **10**, 034101.
150 G. Fei, L. Nie, L. Zhong, Q. Shi, K. Hu, C. Parra-Cabrera, H. Oprins, R. Ameloot and S. Yang, *Mater. Today Commun.*, 2022, **31**, 103482.
151 S. Orsini, M. Lauricella, A. Montessori, A. Tiribocchi, M. Durve, S. Succi, L. Persano, A. Camposeo and D. Pisignano, *Appl. Phys. Rev.*, 2025, **12**, 011306.
152 F. Sommonte, N. Denora and D. A. Lamprou, *Pharmaceuticals*, 2023, **16**, 69.
153 N. Weigel, M. J. Männel and J. Thiele, *ACS Appl. Mater. Interfaces*, 2021, **13**, 31086–31101.
154 F. Kotz, P. Risch, D. Helmer and B. E. Rapp, *Micromachines*, 2018, **9**, 115.

155 G. M. Whitesides, *Nature*, 2006, **442**, 368–373.
156 J. C. McDonald and G. M. Whitesides, *Acc. Chem. Res.*, 2002, **35**, 491–499.
157 S.-Y. Teh, R. Lin, L.-H. Hung and A. P. Lee, *Lab Chip*, 2008, **8**, 198–220.
158 A. S. Utada, E. Lorenceau, D. R. Link, P. D. Kaplan, H. A. Stone and D. A. Weitz, *Science*, 2005, **308**, 537–541.
159 C.-H. Choi, H. Lee, A. Abbaspourrad, J. H. Kim, J. Fan, M. Caggioni, C. Wesner, T. Zhu and D. A. Weitz, *Adv. Mater.*, 2016, **28**, 3340–3344.
160 A. Urrios, C. Parra-Cabrera, N. Bhattacharjee, A. M. Gonzalez-Suarez, L. G. Rigat-Brugarolas, U. Nallapatti, J. Samitier, C. A. DeForest, F. Posas, J. L. Garcia-Cordero and A. Folch, *Lab Chip*, 2016, **16**, 2287–2294.
161 J. Li, D. K. Baxani, W. D. Jamieson, W. Xu, V. G. Rocha, D. A. Barrow and O. K. Castell, *Adv. Sci.*, 2020, **7**, 1901719.
162 M. Zhang, J. Li, S. Liang, Y. Li and H. Chen, *Microfluid. Nanofluid.*, 2025, **29**, 60.
163 M. A. Levenstein, L. A. Bawazer, C. S. Mc Nally, W. J. Marchant, X. Gong, F. C. Meldrum and N. Kapur, *Microfluid. Nanofluid.*, 2016, **20**, 143.
164 B. R. Benson, H. A. Stone and R. K. Prud'homme, *Lab Chip*, 2013, **13**, 4507–4511.
165 M. V. Bandulasena, G. T. Vladisavljević and B. Benyahia, *J. Colloid Interface Sci.*, 2019, **542**, 23–32.
166 A. Gholivand, O. Korculanin, K. Dahlhoff, M. Babaki, T. Dickscheid and M. P. Lettinga, *Lab Chip*, 2024, **24**, 2317–2326.
167 S. ten Klooster, J. van den Berg, C. Berton-Carabin, J. de Ruiter and K. Schroën, *Chem. Eng. Sci.*, 2022, **261**, 117993.
168 S. Shin, S. Cho, R. Song, H. Kim and J. Lee, *Chem. Eng. J.*, 2023, **471**, 144734.
169 M. Vigogne, T. A. Neuendorf, R. Bernhardt and J. Thiele, *J. Polym. Sci.*, 2023, **61**, 1902–1911.
170 J. L. Sanchez Noriega, N. A. Chartrand, J. C. Valdoz, C. G. Cribbs, D. A. Jacobs, D. Poulson, M. S. Viglione, A. T. Woolley, P. M. Van Ry, K. A. Christensen and G. P. Nordin, *Nat. Commun.*, 2021, **12**, 5509.
171 L. A. Pradela Filho, T. R. L. C. Paixão, G. P. Nordin and A. T. Woolley, *Anal. Bioanal. Chem.*, 2024, **416**, 2031–2037.
172 J. T. Toombs, M. Luitz, C. C. Cook, S. Jenne, C. C. Li, B. E. Rapp, F. Kotz-Helmer and H. K. Taylor, *Science*, 2022, **376**, 308–312.
173 I. A. Coates, W. Pan, M. A. Saccone, G. Lipkowitz, D. Ilyin, M. M. Driskill, M. T. Dulay, C. W. Frank, E. S. G. Shaqfeh and J. M. DeSimone, *Proc. Natl. Acad. Sci. U. S. A.*, 2024, **121**, e2405382121.
174 T. Kamperman, L. M. Teixeira, S. S. Salehi, G. Kerckhofs, Y. Guyot, M. Geven, L. Geris, D. Grijpma, S. Blanquer and J. Leijten, *Lab Chip*, 2020, **20**, 490–495.
175 D. Olvera-Trejo and L. F. Velásquez-García, *Lab Chip*, 2016, **16**, 4121–4132.
176 Y.-H. Hwang, J. H. Lee, T. Um and H. Lee, *Lab Chip*, 2024, **24**, 4778–4785.
177 Y.-H. Hwang, T. Um, G.-N. Ahn, D.-P. Kim and H. Lee, *Chem. Eng. J.*, 2022, **431**, 133998.
178 A. Jans, J. Lölsberg, A. Omidinia-Anarkoli, R. Viermann, M. Möller, L. De Laporte, M. Wessling and A. J. C. Kuehne, *Polymers*, 2019, **11**, 1887.
179 A. Ghaznavi, Y. Lin, M. Douvidzon, A. Szmelter, A. Rodrigues, M. Blackman, D. Eddington, T. Carmon, L. Deych, L. Yang and J. Xu, *Micromachines*, 2022, **13**, 188.
180 J. R. Tumbleston, D. Shirvanyants, N. Ermoshkin, R. Janusziewicz, A. R. Johnson, D. Kelly, K. Chen, R. Pinschmidt, J. P. Rolland, A. Ermoshkin, E. T. Samulski and J. M. DeSimone, *Science*, 2015, **347**, 1349–1352.
181 N. P. Macdonald, J. M. Cabot, P. Smejkal, R. M. Guijt, B. Paull and M. C. Breadmore, *Anal. Chem.*, 2017, **89**, 3858–3866.
182 D. C. Duffy, J. C. McDonald, O. J. A. Schueller and G. M. Whitesides, *Anal. Chem.*, 1998, **70**, 4974–4984.
183 B. Venzac, *Lab Chip*, 2025, **25**, 2129–2147.
184 A. J. L. Morgan, L. Hidalgo San Jose, W. D. Jamieson, J. M. Wymant, B. Song, P. Stephens, D. A. Barrow and O. K. Castell, *PLoS One*, 2016, **11**, e0152023.
185 E. Stolovicki, R. Ziblat and D. A. Weitz, *Lab Chip*, 2018, **18**, 132–138.
186 Y.-H. Hwang, T. Um, J. Hong, G.-N. Ahn, J. Qiao, I. S. Kang, L. Qi, H. Lee and D.-P. Kim, *Adv. Mater. Technol.*, 2019, **4**, 1900457.
187 J. M. Zhang, X. Li, Q. Ji, S. T. Thoroddsen and H. Duan, *Chem. Eng. J.*, 2025, **508**, 160843.
188 K. C. Bhargava, B. Thompson and N. Malmstadt, *Proc. Natl. Acad. Sci. U. S. A.*, 2014, **111**, 15013–15018.
189 R. Song, M. S. Abbasi and J. Lee, *Microfluid. Nanofluid.*, 2019, **23**, 92.
190 Y. Morimoto, M. Kiyosawa and S. Takeuchi, *Sens. Actuators, B*, 2018, **274**, 491–500.
191 J. M. Zhang, A. A. Aguirre-Pablo, E. Q. Li, U. Buttner and S. T. Thoroddsen, *RSC Adv.*, 2016, **6**, 81120–81129.
192 S. Jaligama and J. Kameoka, *J. Mater. Sci.*, 2019, **54**, 14233–14242.
193 J. Zhang, W. Xu, F. Xu, W. Lu, L. Hu, J. Zhou, C. Zhang and Z. Jiang, *J. Food Eng.*, 2021, **290**, 110212.
194 T. Femmer, A. Jans, R. Eswein, N. Anwar, M. Moeller, M. Wessling and A. J. C. Kuehne, *ACS Appl. Mater. Interfaces*, 2015, **7**, 12635–12638.
195 D. Mottin, T. M. Ho and P. A. Tsai, *Rapid Prototyp. J.*, 2021, **27**, 1693–1699.
196 M. B. Romanowsky, A. R. Abate, A. Rotem, C. Holtze and D. A. Weitz, *Lab Chip*, 2012, **12**, 802–807.
197 H. H. Kim, Y. Cho, D. Baek, K. H. Rho, S. H. Park and S. Lee, *Small*, 2022, **18**, 2205001.
198 C.-F. Deng, Y.-Y. Su, S.-H. Yang, Q.-R. Jiang, R. Xie, X.-J. Ju, Z. Liu, D.-W. Pan, W. Wang and L.-Y. Chu, *Lab Chip*, 2022, **22**, 4962–4973.
199 H. Zhang, L. Zhang, C. An, Y. Zhang, F. Shao, Y. Gao, Y. Zhang, H. Li, Y. Zhang, C. Ren, K. Sun, W. He, F. Cheng, H. Wang and D. A. Weitz, *Biofabrication*, 2022, **14**, 035015.
200 X. Leng, W. Zhang, C. Wang, L. Cui and C. J. Yang, *Lab Chip*, 2010, **10**, 2841–2843.

201 J. Ma, G. Tran, A. M. D. Wan, E. W. K. Young, E. Kumacheva, N. N. Iscove and P. W. Zandstra, *Sci. Rep.*, 2021, **11**, 6777.
202 R. Ghosh, A. Arnheim, M. van Zee, L. Shang, C. Soemardy, R.-C. Tang, M. Mellody, S. Baghdasarian, E. Sanchez Ochoa, S. Ye, S. Chen, C. Williamson, A. Karunaratne and D. Di Carlo, *Anal. Chem.*, 2024, **96**, 7817–7839.
203 Z. Wei, M. Zhu, N. Morin, D. Wollsten, J. Hirvonen, X. Yang, H. A. Santos and W. Li, *Adv. Funct. Mater.*, 2025, **35**, 2417307.
204 I. S. Pires, E. Gordon, H. Suh, D. J. Irvine and P. T. Hammond, *Adv. Funct. Mater.*, 2025, **35**, 2503965.
205 K. Sun, J. Zeng, Y. Liu, Z. Zhou, J. Chen, J. Chen, X. Huang, F. Gao, X. Wang, X. Zhang, X. Wang, S. Eeltink and B. Zhang, *Angew. Chem., Int. Ed.*, 2025, **64**, e202418642.
206 L. Mazutis, J. Gilbert, W. L. Ung, D. A. Weitz, A. D. Griffiths and J. A. Heyman, *Nat. Protoc.*, 2013, **8**, 870–891.
207 K. Matuła, F. Rivello and W. T. S. Huck, *Adv. Biosyst.*, 2020, **4**, 1900188.
208 F. Zheng, R. Tian, H. Lu, X. Liang, M. Shafiq, S. Uchida, H. Chen and M. Ma, *Small*, 2024, **20**, 2401400.
209 M. Fletcher, J. Zhu, R. Rubio-Sánchez, S. E. Sandler, K. A. Nahas, L. D. Michele, U. F. Keyser and R. Tivony, *ACS Nano*, 2022, **16**, 17128–17138.
210 C. Hu, H. Chen, J. Zheng, S. Zhou, X. Yang, K. Ngocho, T. Xie, K. Wang and J. Liu, *Adv. Funct. Mater.*, 2025, **35**, 2412408.
211 B. Emde, K. Niehaus and L. Tickenbrock, *Int. J. Mol. Sci.*, 2025, **26**, 497.
212 H. Shafique, V. Karamzadeh, G. Kim, M. L. Shen, Y. Morocz, A. Sohrabi-Kashani and D. Juncker, *Lab Chip*, 2024, **24**, 2774–2790.
213 T.-Y. Lin, T. T. Pfeiffer and P. B. Lillehoj, *RSC Adv.*, 2017, **7**, 37374–37379.
214 N. Azim, J. F. Orrico, D. Appavoo, L. Zhai and S. Rajaraman, *RSC Adv.*, 2022, **12**, 25605–25616.
215 P. Kanitthamniyom, A. Zhou, S. Feng, A. Liu, S. Vasoo and Y. Zhang, *Microsyst. Nanoeng.*, 2020, **6**, 48.
216 M. J. Männel, N. Weigel, N. Hauck, T. Heida and J. Thiele, *Adv. Mater. Technol.*, 2021, **6**, 2100094.
217 A. R. Abate, J. Thiele, M. Weinhart and D. A. Weitz, *Lab Chip*, 2010, **10**, 1774–1776.
218 L. Li, Z. Yan, M. Jin, X. You, S. Xie, Z. Liu, A. van den Berg, J. C. T. Eijkel and L. Shui, *ACS Appl. Mater. Interfaces*, 2019, **11**, 16934–16943.
219 H. Liu, J. A. Piper and M. Li, *Anal. Chem.*, 2021, **93**, 10955–10965.
220 Y. Aslan, O. McGleish, J. Reboud and J. M. Cooper, *Lab Chip*, 2023, **23**, 5173–5179.
221 S.-H. Kim and D. A. Weitz, *Angew. Chem., Int. Ed.*, 2011, **50**, 8731–8734.
222 K. Xu, X.-H. Ge, J.-P. Huang, Z.-X. Dang, J.-H. Xu and G.-S. Luo, *RSC Adv.*, 2015, **5**, 46981–46988.
223 L. Jeon, Y. Kim, J. Yoon, H. Seo and H. Lee, *Small Struct.*, 2023, **4**, 2300200.
224 H.-S. Jeong, E. Kim, J. P. Park, S.-J. Lee, H. Lee and C.-H. Choi, *J. Controlled Release*, 2023, **356**, 337–346.
225 H. Seo and H. Lee, *Nat. Commun.*, 2022, **13**, 5179.
226 H.-S. Jeong, E. Kim, C. Nam, Y. Choi, Y.-J. Lee, D. A. Weitz, H. Lee and C.-H. Choi, *Adv. Funct. Mater.*, 2021, **31**, 2009553.
227 T. W. Cowell, W. Jing, H. Noh and H.-S. Han, *Small*, 2024, **20**, 2404121.
228 M. Rana, R. Ahmad and A. F. Taylor, *Lab Chip*, 2023, **23**, 4504–4513.
229 N. Nuti, P. Rottmann, A. Stucki, P. Koch, S. Panke and P. S. Dittrich, *Angew. Chem., Int. Ed.*, 2022, **61**, e202114632.
230 N. S. Mohd Isa, H. El Kadri, D. Vigolo and K. Gkatzionis, *RSC Adv.*, 2021, **11**, 7738–7749.
231 M. Bakouei, A. Kalantarifard, I. Sundara Raju, T. Avsievich, L. Rannaste, M. Kreivi and C. Elbuken, *Microsyst. Nanoeng.*, 2024, **10**, 183.
232 J. H. Lee, Y.-H. Hwang, M. Noh, J. H. Lee, J. B. Lee and H. Lee, *Biomater. Sci.*, 2023, **11**, 7531–7540.
233 J. H. Lee, Y. S. Kim and H. Lee, *Small Struct.*, 2025, **6**, 2500324.
234 Y. Ding, G. Zoppi, G. Antonini, R. Geiger and A. J. deMello, *Anal. Chem.*, 2024, **96**, 14809–14818.
235 F. Qu, S. Zhao, G. Cheng, H. Rahman, Q. Xiao, R. W. Y. Chan and Y.-P. Ho, *Microsyst. Nanoeng.*, 2021, **7**, 38.
236 M. Fletcher and Y. Elani, *ACS Nano*, 2025, **19**, 13768–13778.
237 H. Seo and H. Lee, *Adv. Sci.*, 2024, **11**, 2305760.
238 J. G. Werner, H. Lee, U. Wiesner and D. A. Weitz, *ACS Nano*, 2021, **15**, 3490–3499.
239 X. Ma, Y. Han, Y.-S. Zhang, Y. Geng, A. Majumdar and J. P. F. Lagerwall, *Nat. Commun.*, 2024, **15**, 1404.
240 Y. Wang, T. Du, X. Hao, Y. Wang, F. Yang, H. He, M. Yang, M. Hong, G. Wang, H. Liu and J. Guo, *Adv. Mater. Technol.*, 2024, **9**, 2301697.
241 J.-W. Kim, Y. Oh, S. Lee and S.-H. Kim, *Adv. Funct. Mater.*, 2022, **32**, 2107275.
242 A. Lashkaripour, D. P. McIntyre, S. G. K. Calhoun, K. Krauth, D. M. Densmore and P. M. Fordyce, *Nat. Commun.*, 2024, **15**, 83.
243 J.-W. Kim, S. H. Han, Y. H. Choi, W. M. Hamonangan, Y. Oh and S.-H. Kim, *Lab Chip*, 2022, **22**, 2259–2291.
244 D. A. Walker, J. L. Hedrick and C. A. Mirkin, *Science*, 2019, **366**, 360–364.
245 B. E. Kelly, I. Bhattacharya, H. Heidari, M. Shusteff, C. M. Spadaccini and H. K. Taylor, *Science*, 2019, **363**, 1075–1079.
246 J.-W. Kim, M. J. Allen, E. A. Recker, L. M. Stevens, H. L. Cater, A. Uddin, A. Gao, W. Eckstrom, A. J. Arrowood, G. E. Sanoja, M. A. Cullinan, B. D. Freeman and Z. A. Page, *Nat. Mater.*, 2025, **24**, 1116–1125.
247 K. S. Mason, J.-W. Kim, E. A. Recker, J. M. Nymick, M. Shi, F. A. Stolpen, J. Ju and Z. A. Page, *ACS Cent. Sci.*, 2025, **11**, 975–982.
248 F. Hormozinezhad, C. Barnes, A. Fabregat, S. Cito and F. Del Giudice, *Lab Chip*, 2025, **25**, 1681–1693.
249 S. Shin, O. D. Land, W. D. Seider, J. Lee and D. Lee, *Small*, 2025, **21**, 2412099.
250 Y. Zhang, M. Li, T.-M. Tseng and U. Schlichtmann, *Commun. Eng.*, 2024, **3**, 71.